

## Wind-driven internal waves and Langmuir circulations in a numerical ocean model of the southern Baltic Sea

Lars B. Axell

Swedish Meteorological and Hydrological Institute, Norrköping, Sweden

Received 13 April 2001; revised 9 January 2002; accepted 16 January 2002; published 27 November 2002.

[1] A one-dimensional numerical ocean model of the southern Baltic Sea is used to investigate suitable parameterizations of unresolved turbulence and compare with available observations. The turbulence model is a  $k$ - $\epsilon$  model that includes extra source terms  $P_{IW}$  and  $P_{LC}$  of turbulent kinetic energy (TKE) due to unresolved, breaking internal waves and Langmuir circulations, respectively. As tides are negligible in the Baltic Sea, topographic generation of internal wave energy (IWE) is neglected. Instead, the energy for deepwater mixing in the Baltic Sea is provided by the wind. At each level the source term  $P_{IW}$  is assumed to be related to a vertically integrated pool of IWE,  $E_0$ , and the buoyancy frequency  $N$  at the same level, according to  $P_{IW}(z) \propto E_0 N^\delta(z)$ . This results in vertical profiles of  $\epsilon$  (the dissipation rate of TKE) and  $K_h$  (the eddy diffusivity) according to  $\epsilon \propto N^\delta$  and  $K_h \propto N^{\delta-2}$  below the main pycnocline. Earlier observations are inconclusive as to the proper value of  $\delta$ , and here a range of values of  $\delta$  is tested in hundreds of 10-year simulations of the southern Baltic Sea. It is concluded that  $\delta = 1.0 \pm 0.3$  and that a mean energy flux density to the internal wave field of about  $(0.9 \pm 0.3) \times 10^{-3} \text{ W m}^{-2}$  is needed to explain the observed salinity field. In addition, a simple wind-dependent formulation of the energy flux to the internal wave field is tested, which has some success in describing the short- and long-term variability of the deepwater turbulence. The model suggests that  $\sim 16\%$  of the energy supplied to the surface layer by the wind is used for deepwater mixing. Finally, it is also shown that Langmuir circulations are important to include when modeling the oceanic boundary layer. A simple parameterization of Langmuir circulations is tuned against large-eddy simulation data and verified for the Baltic Sea. **INDEX TERMS:** 4243 Oceanography: General: Marginal and semienclosed seas; 4544 Oceanography: Physical: Internal and inertial waves; 4572 Oceanography: Physical: Upper ocean processes; 4568 Oceanography: Physical: Turbulence, diffusion, and mixing processes; **KEYWORDS:** Baltic Sea, mixing, turbulence model, Langmuir circulations, internal waves, internal wave energy

**Citation:** Axell, L. B., Wind-driven internal waves and Langmuir circulations in a numerical ocean model of the southern Baltic Sea, *J. Geophys. Res.*, 107(C11), 3204, doi:10.1029/2001JC000922, 2002.

### 1. Introduction

[2] Standard turbulence models such as the commonly used Mellor-Yamada and the  $k$ - $\epsilon$  models [e.g., Mellor and Yamada, 1982; Rodi, 1987] are widely used to model turbulence in surface boundary layers. In general, these turbulence models are forced by buoyancy and resolved velocity shear. Processes such as Langmuir circulations (LC) and internal waves (IW) are subgrid-scale phenomena and must thus be parameterized with extra source terms of turbulent kinetic energy (TKE). It may be argued that coarse-resolution three-dimensional models do, in fact, incorporate some shear due to internal waves. However, since the waves are not properly resolved and the equations usually are hydrostatic, the model-calculated internal wave shear is probably very different from, and unrelated to, the

real shear. Hence the internal wave shear must be parameterized as a subgrid-scale process even in three-dimensional models, today as well as in the near future.

[3] The most popular theory of LC is that of Craik and Leibovich [1976], which explains LC as an instability arising from nonlinear interaction between the Stokes drift and wind-driven currents. Skyllingstad and Denbo [1995] made large-eddy simulations (LES) of LC by adding extra terms due to the Stokes drift in the momentum equations. They showed that LC are very important in the surface boundary layer and that their contribution to the entrainment rate at the base of the mixed layer should be included in turbulence models. In fact, a common problem with turbulence models of the  $k$ - $\epsilon$  type is that they predict too shallow mixed layer depths. For example, see the Baltic Sea halocline depths by Omstedt and Axell [1998]. D'Alessio et al. [1998] included LC in their second-moment turbulence model by adding the Stokes drift to the momentum equations and a vertical velocity due to LC to the vertical

component of the turbulent velocity. They showed that the LC increased the mixed layer depth at Ocean Weather Station Papa by 10–20 m during fall and winter. In this paper, LC will be modeled by adding an extra source term of TKE due to LC.

[4] Traditionally the problem of diffusion in deeper layers has been neglected and only treated by assuming a minimum, constant background level of the vertical diffusion, that is, independent with depth [e.g., *Bryan, 1987; Lehmann, 1995*]. The main reason for this is that its spatial and temporal variations have been largely unknown. In addition, numerical stability in ocean models often requires a minimum background diffusivity. The recent microstructure data of *Toole et al. [1994]* do, however, lend some support to the idea of a background diffusivity that does not vary much with depth, except near rough topography [*Polzin et al., 1997; Stigebrandt, 1999*], despite a varying buoyancy frequency  $N$ , defined by

$$N^2 = -\frac{g}{\rho_0} \frac{\partial \rho}{\partial z}, \quad (1)$$

where  $g$  is the acceleration of gravity,  $\rho$  is density,  $\rho_0$  is a reference density, and  $z$  is the vertical coordinate (positive upward and zero at the surface).

[5] On the other hand, there are other investigations indicating that the eddy diffusivity  $K_h$  decreases with increasing  $N$ , which normally implies an increase with depth below the main pycnocline [*Gargett, 1984; Moun and Osborn, 1986; Stigebrandt and Aure, 1989*]. Accordingly, a parameterization that often has been used in numerical ocean models is

$$K_h = a_0 N^{-1} \quad (2)$$

[*Stigebrandt, 1987; Omstedt, 1990; Cummins et al., 1990; Hu, 1996*] to ensure increased deepwater mixing with depth as  $N$  decreases. A range of suitable values of  $a_0$  for the open ocean seems to be  $(1-2) \times 10^{-7} \text{ m}^2 \text{ s}^{-2}$  [*Gargett, 1984; Stigebrandt, 1987; Axell, 1998*].

[6] A physical interpretation of equation (2) can be obtained in the following way. Combining the well-known Osborn formula

$$K_h \propto \frac{\varepsilon}{N^2}$$

[*Osborn, 1980*] with the common turbulence scaling

$$K_h \propto \frac{k^2}{\varepsilon}$$

[e.g., *Rodi, 1980, p. 27*], we see the diffusivity scales as

$$K_h \sim kN^{-1}. \quad (3)$$

In equation (3),  $k$  denotes TKE density (unit:  $\text{J kg}^{-1}$ ), and  $\varepsilon$  denotes its dissipation rate (unit:  $\text{W kg}^{-1}$ ). Comparing equations (2) and (3), we see that  $a_0$  in (2) is related to the mean background level of the TKE due to unresolved shear. In most turbulence models,  $k$  is calculated in each time step

from the resolved shear, and the effect of internal waves according to equations (2) and (3) could thus in principle be included. As mentioned above, however, since the important small-scale shear production of TKE is usually not resolved in operational oceanographic models and models intended for climate simulations, the model-calculated value of  $k$  below the shear-dominated surface mixed layer is usually much too low to represent the deep mixing. This is because it is not possible to resolve all scales of motion that are responsible for the mixing in the ocean. For instance, to resolve even the longest internal waves properly, the horizontal resolution would have to be of the order of a few hundred meters, and the vertical resolution would have to be less than a meter at all vertical levels. To resolve baroclinic structures such as eddies, a similar resolution is needed.

[7] The diffusion below the mixed layer caused by small-scale shear must thus be parameterized as a subgrid-scale process, for example, by prescribing a carefully chosen minimum value of  $k$  to mimic equation (2). A physically more appealing way is to include and parameterize an extra source term of TKE due to unresolved processes, as was done by *Mellor [1989]* and *Liungman [2000]*. This approach will be followed here and will be described in greater detail in sections 3.6 and 5.2.

[8] The two dominating forcings of deep mixing are the wind and the tide. The energy flux from the barotropic tide interacting with local topography has been investigated by, for example, *Bell [1975]* and *Sjöberg and Stigebrandt [1992]* and has support from observations showing increased levels of the dissipation rate of TKE near rough topography [*Polzin et al., 1997; Stigebrandt, 1999*]. To be able to parameterize wind generation of deep turbulence, it is a good idea to study the Baltic Sea (see Figure 1), since tides are negligible there. Hence the diffusion below the Baltic thermocline is mainly wind-driven, which is supported by indirect observations of the diffusivity showing that  $K_h$  and the vertical energy flux associated with the diffusion have seasonal variabilities in phase with the wind energy [*Axell, 1998*].

[9] The present paper has three goals. The first goal is to present a simple way of including the effects of LC in the  $k$ - $\varepsilon$  turbulence model. As observations in the world oceans seem to be inconclusive as to the proper depth dependence of the mixing below the main pycnocline, the second goal is to find out which depth dependence suits the Baltic Sea best. The third and final goal is to find out how much energy is needed for the Baltic deep mixing. As deep mixing is a relatively slow process, it was decided to simulate a rather long period, 1985–1995. Special emphasis will be on comparison between modeled and calculated long-term development of intermediate to deep stratification. In addition, comparisons will be made with the small amount of available indirect observations of diffusivity and energy fluxes [*Axell, 1998*].

## 2. Description of the Area

[10] The Baltic Sea is a large estuary with positive water balance connected with the world oceans only via the Danish Sounds (see Figure 1), which constitute three rather narrow and shallow channels. The high-saline water enter-

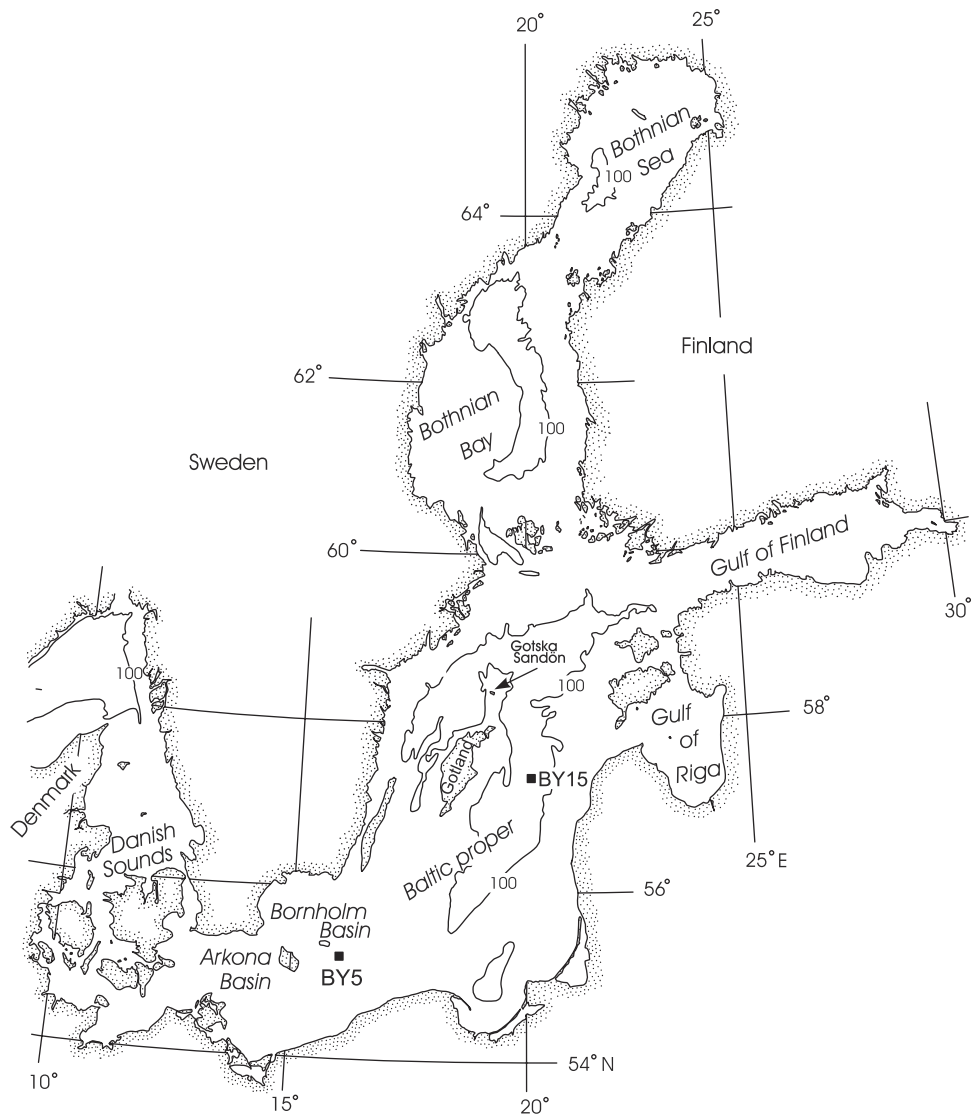


**Figure 1.** Map of the Baltic Sea, including the different subbasins, the two hydrographic stations BY5 and BY15, and the meteorological synop station at Gotska Sandön.

ing through the Danish Sounds forms a rotating, baroclinic bottom pool in the 50 m deep Arkona Basin [Liljebladh and Stigebrandt, 1996]. The bottom pool leaks water into the Bornholm Basin, which is about 100 m deep, where it again forms a pool of dense bottom water. What is stopping the dense water from entering the Baltic proper is a sill of  $\sim 60$  m depth, and it is only when the pool in the Bornholm Basin fills up to this level that the relatively high-saline water can enter the deeper subbasins northeast of the Bornholm Basin. These inflows are very intermittent [Beszczynska-Möller, 1998], and it is only rarely that really high-saline water can enter the Baltic proper as a dense bottom current and reach the deepest parts. An indication of this are the long periods with little or no oxygen in the near-bottom layer [Stigebrandt, 1987; Axell, 1998]. Figure 2 shows observed bottom salinity at the hydrographic station BY15 in the central Baltic proper during 1981–1998; see the map in Figure 1. As the deep water of the Baltic proper is salinity stratified, an inflow of a dense bottom current normally shows up as an increase in bottom salinity. A few

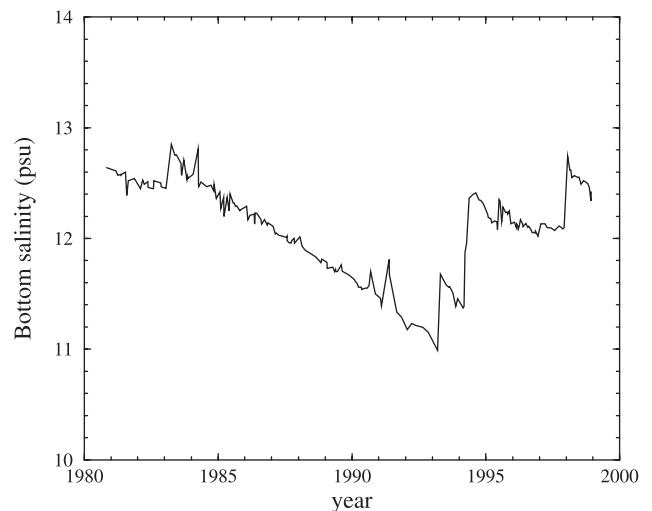


**Figure 2.** Observed bottom salinity at the hydrographic station BY15 in the Baltic proper.

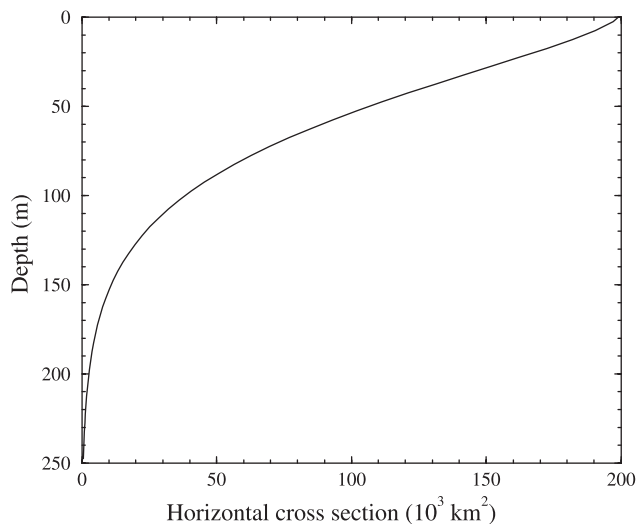


**Figure 3.** Hypsography of the model basin.

large inflows can be detected in Figure 2 in the winters of 1983, 1993, 1994, and 1998. Even though the really dense inflows are rare, they are very important for the dynamics and vertical circulation of the Baltic Sea on the timescale of several years. Between the inflows the bottom salinity decreases because of wind-driven deepwater mixing.

[11] The river runoff entering the Baltic Sea mixes with the more saline water below and flows out of the Baltic Sea as a surface current of brackish water through the Danish Sounds. The outflowing water then mixes with the high-saline water north of the Danish Sounds, and

some of it reenters the Baltic Sea as a dense bottom current.

### 3. Numerical Model

#### 3.1. Simplifying Assumptions

[12] The model domain is the southern Baltic Sea, including Baltic proper up to  $\sim 60^\circ\text{N}$ , Gulf of Finland, and Gulf of Riga; see the map in Figure 1. To make the investigation as clear-cut and easy to interpret as possible, it was decided to use a single-basin one-dimensional numerical ocean model. It is horizontally homogeneous but with a high vertical resolution, and a simple sea-ice model is included. As for the depth distribution of the horizontal cross section of the model basin, a simple analytical expression was used, which is fairly representative of the actual hypsography; see Figure 3. Here it is assumed that the model domain can be represented by the hydrographic station BY15 [cf. *Rahm*, 1988; *Winsor et al.*, 2001]. It is situated in the deepest part of a subbasin in the Baltic proper, where the maximum depth is 249 m. All observed profiles of salinity and temperature in this study are from BY15, which were also used to determine suitable initial conditions for the model. It was also assumed that the atmospheric forcing was horizontally homogeneous enough that it could be represented by observations made at Gotska Sandön in the northern Baltic proper (see Figure 1).

#### 3.2. River Runoff

[13] Monthly mean values of the river runoff,  $Q_{\text{river}}$ , to the model domain were used, which were extracted from a database of observed river runoff at the Swedish Meteorological and Hydrological Institute (SMHI); see Figure 4.

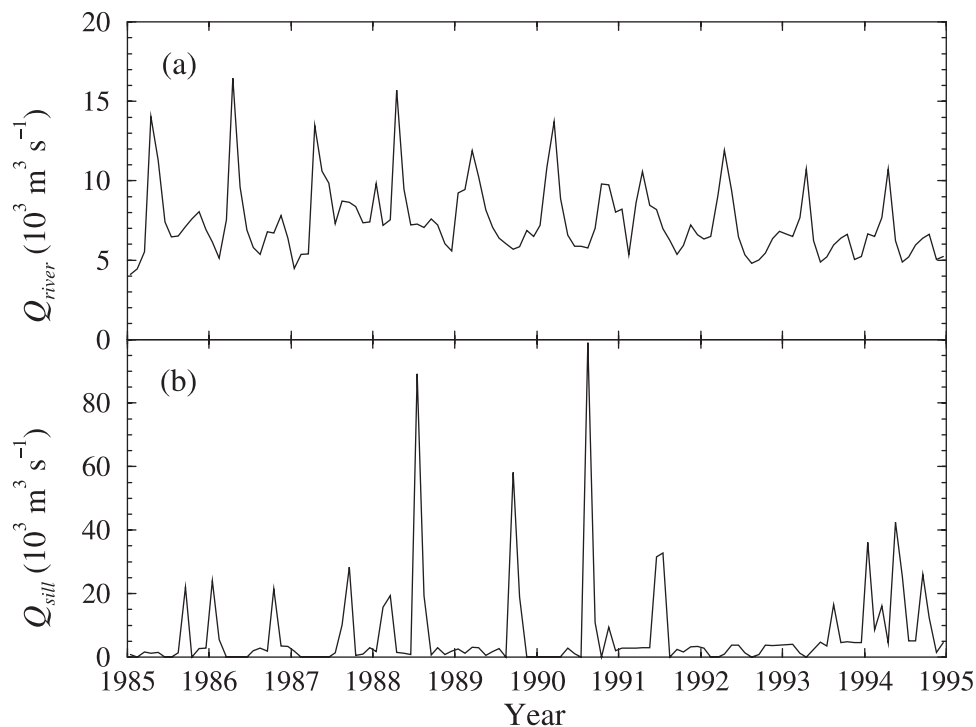


**Figure 4.** Time series of (a) observed river runoff to the model domain,  $Q_{\text{river}}$  and (b) calculated deep inflow at the sill,  $Q_{\text{sill}}$ . The 10-year mean values are  $7400$  and  $6600 \text{ m}^3 \text{ s}^{-1}$ , respectively.

The long-term mean was  $7400 \text{ m}^3 \text{ s}^{-1}$ , which is about half of the long-term mean for the whole Baltic Sea. Most of the other half of the river runoff flows into the subbasins north of the model domain, where it mixes with underlying water. The resulting brackish surface water in these northern subbasins is then exported as a baroclinic flow into, and mixed with, the surface water of the model domain, that is, the Baltic proper.

[14] The light surface water may then be mixed with the water below during wind events, especially storms which regularly take place during fall. To some extent, the near-surface turbulence may be trapped near the surface because of the shallow halocline (20–30 m deep) generated by the brackish inflow, until the turbulence becomes intense enough to penetrate the shallow halocline. These features are visible in observations as well as in model results (not shown). Shallow summer thermoclines have the same effect on the turbulence.

### 3.3. Baroclinic Inflows and Outflows and Dense Bottom Currents

[15] The baroclinic inflow of brackish surface water from the subbasins north of the model domain,  $Q_{\text{north}}$ , was assumed to be  $44,400 \text{ m}^3 \text{ s}^{-1}$  [Wulff and Stigebrandt, 1989] and constant in time. Because the inflowing water has lower density than the surface water of the modeled basin, it was assumed that the inflow takes place at a level near the surface. The temperature of the inflowing water was assumed to be equal to the modeled sea surface temperature. The salinity of the inflow was assumed to be 5.6 practical salinity unit (psu), which is the long-term mean surface salinity in the area just north of the Baltic proper. Some of the Baltic proper surface water is destined to become deep water in the subbasins north of the model domain, but this flow is included in the total outflow of surface water from the model; see equation (8).

[16] Although some of the brackish surface water tends to stay near the coasts because of the Coriolis effect, a large fraction is spread by lateral mixing and advection into the central parts of the Baltic proper. The monthly lateral spreading rate of juvenile freshwater in the Baltic proper was calculated from hydrographic data by *Eilola and Stigebrandt* [1998]. It is judged that it is a fair simplification to use a horizontally integrated model in this study. An obvious drawback, of course, is that the lateral distribution of the brackish surface water cannot be resolved. The observations, however, are from the central Baltic proper, and not horizontally averaged; see the map in Figure 1.

[17] Unfortunately, deep inflows and the resulting bottom currents are difficult to model in terms of timing, strength, and salinity. Even though the really dense bottom currents that reach the deepest parts of the Baltic proper are rare, they cannot be neglected on the timescale of several years; see Figure 2. Moreover, the halocline at  $\sim 100$  m depth is usually ventilated every year as a result of medium-deep inflows [Stigebrandt, 1987; Elken, 1996], and this, of course, affects the stratification at intermediate depths. In this paper the deepwater inflow into the Baltic proper was estimated with a simple model for baroclinic flow over a sill using the observed stratification at the hydrographic station

BY5 in the Bornholm Basin; see the map in Figure 1. Assuming that the inflow  $Q_{\text{sill}}$  over the sill in the Bornholm Basin is controlled by rotation, we have

$$Q_{\text{sill}} = \frac{g\Delta\rho}{2f}(D_{\text{sill}} - D_{ml})^2,$$

which can be shown by integrating Margules' relation [cf. Gill, 1982, p. 219]. Here  $\Delta\rho$  is the observed density difference between the upper and the lower layer, and  $f$  is the Coriolis parameter.  $D_{\text{sill}} = 60$  m is the sill depth, and  $D_{ml}$  is the depth of the mixed layer in the Bornholm Basin, calculated as the depth where the observed density gradient has a maximum. Whenever  $D_{ml} > D_{\text{sill}}$ ,  $Q_{\text{sill}}$  is set to zero. The calculated values of  $Q_{\text{sill}}$  and its salinity and temperature were interpolated in time every second day before monthly mean values were calculated; see Figure 4.

[18] Initially, the dense bottom current originating at the sill is assumed to have the same salinity and temperature as the water at sill depth in the Bornholm Basin. Because of entrainment of ambient water in the Baltic proper, the density decreases while the volume flow increases. Normally, the salinity decreases in the bottom current, whereas the temperature can either decrease or increase. The model for the bottom current is identical to that by *Stigebrandt* [1987], and only a short summary will be given here. The normalized volume flow  $q$  is given by

$$q = \frac{Q}{B},$$

where  $Q$  is the total flow (in  $\text{m}^3 \text{ s}^{-1}$ ) and  $B$  is the constant width of the current. The current velocity  $u_d$  is then given by

$$u_d = \left( \frac{sqg'}{C_d^b} \right)^{1/3},$$

where  $s$  is the constant slope and  $C_d^b$  is the bottom drag coefficient.  $g'$  is the reduced gravity according to

$$g' = g \frac{\Delta\rho}{\rho_0},$$

where  $\Delta\rho$  is the density difference between the bottom current and the surrounding water (in the model basin) at the depth of the current. The equations governing the changes in volume flow, salinity, and temperature in the bottom current are

$$dq = 2m_0su_d(C_d^b)^{1/2}dx, \quad (4)$$

$$dS_d = (S_a - S_d) \frac{dq}{q + dq}, \quad (5)$$

$$dT_d = (T_a - T_d) \frac{dq}{q + dq}, \quad (6)$$

where  $m_0$  is a constant,  $dx$  is the along-stream coordinate increment, and  $dq$ ,  $dS_d$ , and  $dT_d$  are the calculated

**Table 1.** Coefficients and Constants Used in This Paper

Notation	Description	Value	Unit
$A_0$	surface area of the model domain	$1.99 \times 10^{11}$	$\text{m}^2$
$B$	width of the bottom current	$2.5 \times 10^4$	m
$C_d^b$	bottom drag coefficient	$3.0 \times 10^{-3}$	–
$c_{\varepsilon 1}$	coefficient in the turbulence model	1.44	–
$c_{\varepsilon 2}$	coefficient in the turbulence model	1.92	–
$c_{\mu}^0$	coefficient in the turbulence model	0.5562	–
$c_p$	specific heat of sea water	$4.19 \times 10^3$	$\text{J kg}^{-1} \text{K}^{-1}$
$c_{f1}$	coefficient in equation for $T_f$	$-5.75 \times 10^{-2}$	$\text{K psu}^{-1}$
$c_{f2}$	coefficient in equation for $T_f$	$1.71 \times 10^{-3}$	$\text{K psu}^{-3/2}$
$c_{f3}$	coefficient in equation for $T_f$	$-2.15 \times 10^{-4}$	$\text{K psu}^{-2}$
$c_{p1}$	coefficient in equation of state	$7.18 \times 10^{-6}$	$\text{K}^{-2}$
$c_{p2}$	coefficient in equation of state	$8 \times 10^{-4}$	$\text{psu}^{-1}$
$f$	Coriolis parameter	$1.2 \times 10^{-4}$	$\text{s}^{-1}$
$H$	basin depth	250	m
$\kappa$	von Karman's constant	0.4	–
$k_i$	thermal conductivity of ice	2.0	$\text{W m}^{-1} \text{K}^{-1}$
$k_s$	thermal conductivity of snow	0.3	$\text{W m}^{-1} \text{K}^{-1}$
$L_i$	heat of fusion for ice	$3.34 \times 10^5$	$\text{J kg}^{-1}$
$m_0$	entrainment coefficient	0.6	–
$\nu$	kinematic viscosity	$1.3 \times 10^{-6}$	$\text{m}^2 \text{s}^{-1}$
$\rho_i$	density of sea ice	910	$\text{kg m}^{-3}$
$\rho_0$	reference density of sea water	$1.0 \times 10^3$	$\text{kg m}^{-3}$
$s$	bottom slope of the bottom current	$6.0 \times 10^{-4}$	–
$\sigma_\varepsilon$	turbulent Schmidt number for $\varepsilon$	1.08	–
$\sigma_k$	turbulent Schmidt number for $k$	1.0	–
$V$	total volume of the model basin	$1.3 \times 10^{13}$	$\text{m}^3$

increments of volume flow, salinity, and temperature, respectively.  $S$  and  $T$  denote salinity and temperature, respectively, and indices  $d$  and  $a$  refer to the dense bottom current and the ambient water, respectively. For further details concerning the derivation of the equations, see *Stigebrandt* [1987]. The values of the coefficients above are given in Table 1.

[19] The three equations (4)–(6) were integrated until maximum depth of the model basin ( $H = 250$  m) was reached or when the density difference between the bottom current and the ambient water at that depth became zero. The resulting flow  $Q_{\text{deep}}$  was then interleaved at the appropriate depth in the model basin. The computed mean inflow from the Bornholm Basin,  $Q_{\text{sill}}$ , was  $\sim 6600 \text{ m}^3 \text{ s}^{-1}$  (see Figure 4), and after entrainment the mean volume flow was  $\sim 13,000 \text{ m}^3 \text{ s}^{-1}$  for the modeled period. At a certain time step, the model calculates a single interleaving depth for the bottom current. However, by running the model for an extended period of time, the slowly changing upstream conditions in the Bornholm Basin and in the model basin imply changing interleaving depths. For the time period 1985–1995, only a fraction of the inflow from the Bornholm Basin was dense enough to reach the deepest part of the Baltic proper. On the average, however, the modeled currents reached  $\sim 100$  m depth, in accordance with observations [*Elken*, 1996, p. 23].

[20] The total inflow of water to the basin,  $Q_{\text{in}}$ , is given by

$$Q_{\text{in}} = Q_{\text{north}} + Q_{\text{deep}} + Q_{\text{river}} + P_{\text{net}}A_0, \quad (7)$$

where  $P_{\text{net}}$  is the net precipitation, that is, precipitation minus evaporation (see below), and  $A_0$  is the surface area of the model domain. The total outflow from the model

domain,  $Q_{\text{out}}$ , is assumed to be in balance with  $Q_{\text{in}}$ , that is,

$$Q_{\text{out}} = Q_{\text{in}}, \quad (8)$$

and assumed to take place at the surface.

### 3.4. Hydrodynamic Model Equations

[21] The transport equations for horizontal momentum are

$$\frac{\partial(\rho u)}{\partial t} + w \frac{\partial(\rho u)}{\partial z} = \frac{\partial}{\partial z} \left[ K_m \frac{\partial(\rho u)}{\partial z} \right] + f \rho v, \quad (9)$$

$$\frac{\partial(\rho v)}{\partial t} + w \frac{\partial(\rho v)}{\partial z} = \frac{\partial}{\partial z} \left[ K_m \frac{\partial(\rho v)}{\partial z} \right] - f \rho u, \quad (10)$$

where  $\rho$  is the density of seawater and  $u$ ,  $v$ , and  $w$  are eastward, northward, and upward velocities, respectively. Further,  $t$  is time, and  $K_m$  is the eddy viscosity. The vertical velocity is due to inflows and outflows at that level and are calculated according to

$$Q_z^i = Q_z^{i-1} + Q_{\text{in}}^i - Q_{\text{out}}^i,$$

$$w(z) = \frac{Q_z^i}{A^i},$$

where  $Q_z$  is the vertical volume flux upward, index  $i$  denotes the discrete depth level (increasing upward), and  $A$  is the horizontal cross section.

[22] The upper boundary conditions for the momentum equations are

$$K_m \frac{\partial(\rho u)}{\partial z} = \tau_x, \quad (11)$$

$$K_m \frac{\partial(\rho v)}{\partial z} = \tau_y. \quad (12)$$

In the above,  $\tau_x$  and  $\tau_y$  are the eastward and northward components, respectively, of the stresses at the boundaries due to wind or ice drift, calculated with stability-dependent bulk formulas according to *Launiainen* [1995]. At the bottom the velocity is assumed to be zero.

[23] The transport equation for heat is

$$\frac{\partial(\rho c_p T)}{\partial t} + w \frac{\partial(\rho c_p T)}{\partial z} = \frac{\partial}{\partial z} \left[ K_h \frac{\partial(\rho c_p T)}{\partial z} \right] + \Gamma_{sw} + \Gamma_h, \quad (13)$$

where  $c_p$  and  $T$  are the heat capacity and temperature of seawater, respectively, and  $K_h$  is the eddy diffusivity for heat. Further,  $\Gamma_{sw}$  is a source of heat due to the fraction of shortwave radiation absorbed at that level, and  $\Gamma_h$  is a source or sink of heat due to inflows and outflows; see *Omstedt and Nyberg* [1996].

[24] The upper boundary condition for the ice-free case is

$$K_h \frac{\partial(\rho c_p T)}{\partial z} = F_{\text{net}}, \quad (14)$$

where  $F_{\text{net}}$  is the net heat exchange between the ocean and the atmosphere, that is, the sum of sensible heat flux, latent heat flux, net longwave radiation, and shortwave radiation absorbed in the surface layer.  $F_{\text{net}}$  is defined as positive when directed upward. The heat fluxes are modeled with stability-dependent bulk formulations according to *Launiainen* [1995] with neutral transfer coefficients according to *DeCosmo et al.* [1996].

[25] During ice-covered conditions, the upper boundary temperature is specified to be equal to  $T_f$ , the freezing temperature of sea water:

$$T = T_f(S_{iw}). \quad (15)$$

$T_f$  is calculated with the empirical formula

$$T_f = c_{f1} S_{iw} + c_{f2} S_{iw}^{3/2} + c_{f3} S_{iw}^2 \quad (16)$$

[*Millero*, 1978], where  $S_{iw}$  is the interfacial salinity, that is, the salinity at the ice-water interface as calculated by the model. The values of the coefficients in equation (16) are given in Table 1. At the lower boundary a no-flux condition is used. It should also be mentioned that in the ice-covered case, some of the shortwave radiation is absorbed in the ice and snow, which contributes to the melting; see equation (23).

[26] The transport equation for salinity  $S$  is

$$\frac{\partial S}{\partial t} + w \frac{\partial S}{\partial z} = \frac{\partial}{\partial z} \left( K_s \frac{\partial S}{\partial z} \right) + \Gamma_s, \quad (17)$$

where  $K_s$  is the eddy diffusivity for salt, which is assumed equal to that of heat:

$$K_s = K_h. \quad (18)$$

$\Gamma_s$  is a source or sink of salt due to inflows and outflows at that level, analogous to  $\Gamma_h$  in equation (13) [see *Omstedt and Nyberg*, 1996]. At the surface the boundary condition is

$$K_s \frac{\partial S}{\partial z} = P_{\text{net}} S_s, \quad (19)$$

where  $S_s$  is the sea surface salinity. Here we will assume that  $P_{\text{net}} = 110 \text{ mm yr}^{-1}$  (constant in time), corresponding to a net freshwater inflow of  $670 \text{ m}^3 \text{ s}^{-1}$  [*Omstedt et al.*, 1997]. As in the case of heat, a no-flux boundary condition is used at the bottom. The density is calculated with a simplified equation of state according to

$$\rho = \rho_0 \left[ 1 - c_{\rho 1} (T - T_{\text{max}})^2 + c_{\rho 2} S \right], \quad (20)$$

where  $c_{\rho 1}$  and  $c_{\rho 2}$  are constants (see Table 1), and  $T_{\text{max}}$  is the temperature of maximum density calculated as

$$T_{\text{max}}(z) = 3.98 - 0.223 \times S(z). \quad (21)$$

### 3.5. Ice Model

[27] The ice model is a simplified version of the model used by *Omstedt and Nyberg* [1996]. The difference is that frazil ice, ridging, horizontal advection of ice, and ice concentration are not considered here. During the initial phase of ice growth  $T_s < T_f$  (supercooled water), and the ice grows according to

$$\Delta h_i = \frac{(T_f - T_s) \rho c_p \Delta z}{L_i \rho_i}, \quad (22)$$

where  $\Delta h_i$  is the increase of ice thickness during the current time step, and  $\Delta z$  is the thickness of the uppermost grid cell.  $L_i$  is the heat of fusion for ice, and  $\rho_i$  is the density of sea ice. Hence initially the ice growth is linear in time and proportional to the temperature difference  $T_f - T_s$ . The heat deficit in the water (relative to the freezing temperature  $T_f$ ) is thus turned into an equivalent thickness of ice. Afterward,  $T_s$  is set to  $T_f$ . Once the thickness exceeds 1 mm, however, the ice starts to grow according to

$$\rho_i L_i \frac{dh_i}{dt} = \frac{k_i k_s}{k_i h_s + k_s h_i} (T_f - T'_a) - \Gamma_i - F_w, \quad (23)$$

where  $k_i$  and  $k_s$  are the thermal conductivities for ice and snow, respectively, the snow thickness  $h_s = 0.2 h_i$  (which, of course, is a simplification), and

$$T'_a = \begin{cases} T_a & \text{if } T_a < T_f \\ T_f & \text{otherwise.} \end{cases} \quad (24)$$

The values of coefficients and constants are given in Table 1.  $\Gamma_i$  in equation (23) is a source term of heat due to absorbed shortwave radiation, and  $F_w$  is the heat flux from water to ice calculated from the heat gradient as

$$F_w = K_h \frac{\partial(\rho c_p T)}{\partial z}. \quad (25)$$

Finally, the drag at the ice-water boundary was calculated with standard bulk formulations [e.g., *Omstedt and Nyberg, 1996*], and the ice drift velocity was assumed to be 2% of the wind speed, with an ice-water drag coefficient of 0.0035.

### 3.6. Turbulence Model

[28] The vertical diffusion is calculated with a two-equation model of turbulence, the so-called  $k$ - $\varepsilon$  model [e.g., *Burchard et al., 1998*], in which transport equations for the turbulent kinetic energy  $k$  and its dissipation rate  $\varepsilon$  are solved in each time step. The  $k$ - $\varepsilon$  turbulence model has been applied successfully many times for the Baltic Sea; see for example *Omstedt and Axell [1998]*. In the standard setup of the model, one source of TKE is the current shear resulting from the surface stress due to wind or ice drift. Another source is destabilizing buoyancy flux at the surface due to cooling, evaporation, or salt rejection due to freezing ice. Additional source terms  $P_{LC}$  and  $P_{IW}$  are added to account for Langmuir circulations in the surface mixed layer (see section 4) and unresolved shear below the surface mixed layer, mainly due to internal waves (see section 5).

[29] The transport equation for  $k$  is then given by

$$\frac{\partial k}{\partial t} = \frac{\partial}{\partial z} \left( \frac{K_m}{\sigma_k} \frac{\partial k}{\partial z} \right) + P_s^{tot} + P_b - \varepsilon, \quad (26)$$

where  $\sigma_k$  is the Schmidt number for  $k$ , and  $P_s^{tot}$  represents total shear production, that is,

$$P_s^{tot} = P_s + P_{LC} + P_{IW}. \quad (27)$$

Here  $P_s$  denotes the production due to resolved shear according to

$$P_s = K_m \left[ \left( \frac{\partial u}{\partial z} \right)^2 + \left( \frac{\partial v}{\partial z} \right)^2 \right], \quad (28)$$

and  $P_{LC}$  and  $P_{IW}$  are specified in sections 4 and 5, respectively. The buoyancy production or destruction term  $P_b$  is given by

$$P_b = K_h \frac{g}{\rho_0} \frac{\partial \rho}{\partial z}. \quad (29)$$

[30] The corresponding transport equation for  $\varepsilon$  is

$$\frac{\partial \varepsilon}{\partial t} = \frac{\partial}{\partial z} \left( \frac{K_m}{\sigma_\varepsilon} \frac{\partial \varepsilon}{\partial z} \right) + \frac{\varepsilon}{k} [c_{\varepsilon 1} P_s^{tot} + c_{\varepsilon 3} P_b - c_{\varepsilon 2} \varepsilon], \quad (30)$$

where  $\sigma_\varepsilon$  is the Schmidt number for  $\varepsilon$ . For consistency, the extended shear term  $P_s^{tot}$  (equation (27)) is used also in the equation for  $\varepsilon$ .

[31] Standard values of the empirical coefficients  $\sigma_\varepsilon$ ,  $c_{\varepsilon 1}$ , and  $c_{\varepsilon 2}$  were used; see Table 1. The coefficient  $c_{\varepsilon 3}$  in the buoyancy term requires special attention as it is not a constant. Following *Burchard and Baumert [1995]*, let us derive a relation between  $c_{\varepsilon 3}$  and the steady-state flux Richardson number, in the case of equilibrium between

local sources and sinks in the transport equations for  $k$  and  $\varepsilon$ . We then have

$$P_s^{tot} + P_b = \varepsilon, \quad (31)$$

$$c_{\varepsilon 1} P_s^{tot} + c_{\varepsilon 3} P_b = c_{\varepsilon 2} \varepsilon. \quad (32)$$

Eliminating  $P_s^{tot}$  between equations (31) and (32) and solving for  $c_{\varepsilon 3}$ , we obtain

$$c_{\varepsilon 3} = c_{\varepsilon 1} + (c_{\varepsilon 2} - c_{\varepsilon 1}) \frac{\varepsilon}{P_b}. \quad (33)$$

Now, the (steady-state) flux Richardson number  $R_f$  is the ratio between the local buoyancy destruction and shear production of TKE and may be written

$$R_f = -\frac{P_b}{P_s^{tot}}, \quad (34)$$

which can be used in equation (31) to obtain

$$\frac{\varepsilon}{P_b} = 1 - \frac{1}{R_f}. \quad (35)$$

Using equation (35) in equation (33), we find

$$c_{\varepsilon 3} = c_{\varepsilon 2} - \frac{c_{\varepsilon 2} - c_{\varepsilon 1}}{R_f} \quad (36)$$

[cf. *Burchard and Baumert, 1995*].

[32] From equation (36) we see that, in locally maintained steady turbulence,  $c_{\varepsilon 3}$  is a single-valued function of the flux Richardson number, which in turn depends on the stability and dynamics of the fluid. In stable stratification ( $N^2 > 0$ ), reported values of  $R_f$  range from  $\sim 0.05$  [e.g., *Stigebrandt, 1976; Stigebrandt and Aure, 1989*] in the low end up to  $\sim 0.20$  [e.g., *Ivey and Imberger, 1991*] in the high end. *Arneborg [2000]* showed that  $R_f$  is a factor 2 smaller in patchy turbulence compared with nonpatchy turbulence. The small-scale mixing efficiency  $R_f$  within a turbulent patch is closer to the high-end estimate, but as the fluid in the patch spreads out after the initial mixing event and interleaves into the surrounding fluid, some of the potential energy gained in the previous mixing event is irreversibly lost. The result is that the large-scale value of  $R_f$  is only half of the instantaneous value within the patch. In contrast, as the turbulence in the surface mixed layer is much less patchy than below, the small-scale and large-scale values of  $R_f$  are equal and closer to the high-end estimates. See *Arneborg [2000]* for a more thorough discussion. Here we will assume that the turbulence is patchy (because of intermittent internal wave breaking or sporadic occurrence of deep baroclinic eddies) with  $R_f = 0.08$  if  $P_{IW} > P_s$ , and  $R_f = 0.16$  if  $P_s \geq P_{IW}$ ; see Table 2 and Figure 5. The larger value of  $R_f$  is consistent with the results reported by *Axell and Liungman [2001]*, who found that  $c_{\varepsilon 3} = -1.1$  for near-surface turbulence in stable stratification using the same stability functions as in the present model (see equations (40) and (41) below).

**Table 2.** Choice of Values of  $R_f$  and  $c_{\varepsilon 3}$ 

Case	$R_f$	$c_{\varepsilon 3}$
$N^2 \geq 0, P_s \geq P_{IW}$	0.16	-1.08
$N^2 \geq 0, P_s < P_{IW}$	0.08	-4.08
$N^2 < 0$	<0	+1.0

[33] In unstable stratification ( $N^2 < 0$ ), it has been recommended [Rodi, 1987] that  $c_{\varepsilon 3}$  change sign to ensure a source term for  $\varepsilon$  when  $\partial\rho/\partial z$  changes sign. Simple numerical experiments (not shown) reveal that to maintain turbulence in the case of free convection, we must have  $c_{\varepsilon 3} < c_{\varepsilon 2} = 1.92$ . Rodi [1987] suggested  $c_{\varepsilon 3} = c_{\varepsilon 1} = 1.44$ , but here we will assume  $c_{\varepsilon 3} = 1.0$ , which yields good results [Axell and Liungman, 2001] when simulating convection experiment A by Deardorff *et al.* [1969].

[34] A no-flux boundary condition is used for the turbulent kinetic energy  $k$  at the upper as well as the lower boundary. As for the dissipation rate  $\varepsilon$  a no-flux condition was used at the bottom, whereas at the surface,  $\varepsilon$  was calculated using the law of the wall, which yields

$$\varepsilon = \left(c_{\mu}^0\right)^3 \frac{k^{3/2}}{\kappa d_1}, \quad (37)$$

where  $\kappa = 0.40$  is von Karman's constant, and  $d_1$  is the distance to the center of the uppermost grid cell.

[35] Having calculated  $k$  and  $\varepsilon$ , the eddy viscosity and the eddy diffusivity are calculated from

$$K_m = c_{\mu} \left(c_{\mu}^0\right)^3 \frac{k^2}{\varepsilon}, \quad (38)$$

$$K_h = c'_{\mu} \left(c_{\mu}^0\right)^3 \frac{k^2}{\varepsilon}, \quad (39)$$

where  $c_{\mu}^0$  is a constant in the model.  $c_{\mu}$  and  $c'_{\mu}$  are stability functions, given by

$$c_{\mu} = \frac{c_{\mu}^0 + 0.108R_t}{1 + 0.308R_t + 0.00837R_t^2}, \quad (40)$$

$$c'_{\mu} = \frac{c_{\mu}^0}{1 + 0.277R_t} \quad (41)$$

[Axell and Liungman, 2001]. In equations (40) and (41) we have introduced the turbulent Richardson number  $R_t$ , defined as

$$R_t = \frac{k^2 N^2}{\varepsilon^2}. \quad (42)$$

To ensure a smooth transition into the convective regime, the following smoothing function by Burchard and Petersen [1999] was used:

$$\tilde{R}_t = \max \left[ R_t, R_t - \frac{(R_t - R_t^c)^2}{R_t + R_t^{\min} - 2R_t^c} \right], \quad (43)$$

where  $\tilde{R}_t$  replaces  $R_t$  in equations (40)–(41) when  $R_t < R_t^c$ , and  $R_t^c = -1.0$  and  $R_t^{\min} = -3.0$ .

### 3.7. Numerical Implementation

[36] The model was implemented in the software PROBE [Svensson, 1978, 1998], which is a very flexible one-dimensional equation solver. It has been used successfully many times for simulations of boundary layers in lakes, the atmosphere, and the ocean [e.g., Svensson and Sahlberg, 1989; Nordblom, 1997; Omstedt and Axell, 1998]. In this equation solver, all variables are located at the centers of the grid cells. PROBE has many built-in features to handle different situations, such as time-dependent boundary conditions, varying hypsography, inflows and outflows, different turbulence models, etc.

[37] In all simulations the time step was 150 s, and the grid spacing was 5 m. The minimum values of  $k$  and  $\varepsilon$  were  $1 \times 10^{-10} \text{ m}^2 \text{ s}^{-2}$  and  $1 \times 10^{-10} \text{ m}^2 \text{ s}^{-3}$ , respectively. When the minimum values were reached, laminar values were used for the viscosity and the diffusivity of heat and salt.

## 4. Parameterization of Langmuir Circulations

[38] Langmuir circulations can be described as ordered large-scale vertical motions in the surface layer of the oceans. Although LC have nothing to do with convection, the circulation pattern is rather similar to so-called convective rolls in the atmospheric boundary layer. The detailed physics behind LC is described in, for example, Craik and Leibovich [1976] and will not be repeated here. See also the review by Brown [1980] for examples of similar flows in the atmospheric boundary layer. The prevailing explanation is that LC arise from a nonlinear interaction between the Stokes drift and wind drift currents.

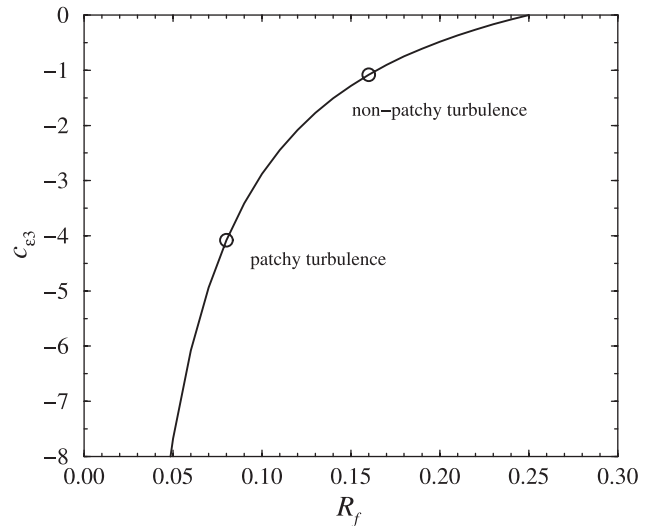


**Figure 5.** Relation between  $c_{\varepsilon 3}$  and steady state flux Richardson number  $R_f$ .

[39] Following *Li and Garrett* [1993], the Stokes drift  $u_s$  for a fully developed sea may be expressed as

$$u_s = 0.016W \exp(z/L_{LC}), \quad (44)$$

where  $W$  is the magnitude of the 10-m wind, and

$$L_{LC} = 0.12 \frac{W^2}{g}. \quad (45)$$

Thus with a wind speed of, say,  $10 \text{ m s}^{-1}$  we see that the Stokes drift itself decays quickly with depth, with an e-folding depth of the order of a meter. The generated Langmuir circulations, however, usually fill up the whole mixed layer [*Skyllingstad and Denbo*, 1995].

[40] *D'Alessio et al.* [1998] added extra terms for the Stokes drift in the Coriolis terms in the momentum equations and added the extra contribution of the shear of the Stokes drift in the TKE equation. In addition, they added an extra contribution to the vertical turbulent velocity in their model. A similar approach will be tested here with the  $k-\epsilon$  model, but as the contribution from the Stokes drift itself proved negligible, it will be neglected here. The whole effect of the LC will be included in a single term for the production of TKE, which enters in the equation for  $k$  as well as for  $\epsilon$ .

[41] A physically appealing velocity scale for  $w_{LC}$  is  $(u_* u_s)^{1/2}$ , the so-called Craik-Leibovich velocity scale [*Leibovich*, 1983; *Plueddemann et al.*, 1996], where  $u_* = (\tau/\rho)^{1/2}$  is the friction velocity, and  $\tau$  is the wind stress.  $u_*$  represents the effect of the wind drift current and  $u_s$  the state of the surface wave field. However, if no information about the wave field is available (which is the case in this study), we may as well assume that  $u_s$  is related to the wind forcing directly, as  $u_s \propto W$  according to equation (44), and assume that  $w_{LC} \propto u_s$ .

[42] As for the vertical variation of  $w_{LC}$ , it is reasonable that it is zero at the surface as well as at a finite depth  $H_{LC}$ , which is often close to the mixed layer depth [*Skyllingstad and Denbo*, 1995; *Gnanadesikan and Weller*, 1995; *Gnanadesikan*, 1996]. For reasons of simplicity it was assumed that

$$w_{LC} = \begin{cases} c_{LC} u_s \sin\left(-\frac{\pi z}{H_{LC}}\right) & \text{if } -z \leq H_{LC}, \\ 0 & \text{otherwise.} \end{cases} \quad (46)$$

The sine function was also suggested by the work of *Gnanadesikan and Weller* [1995] and *Gnanadesikan* [1996] as a first-order profile for the Langmuir cell structures.

[43] Here it will be assumed that  $H_{LC}$  is the depth to which a water parcel with kinetic energy  $u_s^2/2$  can reach on its own by converting its kinetic energy to potential energy, according to

$$-\int_{-H_{LC}}^0 N^2(z) dz = \frac{1}{2} u_s^2. \quad (47)$$

*Bougeault and Lacarrère* [1989] used a similar formula to estimate a turbulent length scale in their turbulence model. By making an analogy with the characteristic convective velocity scale [e.g., *D'Alessio et al.*, 1998], it was finally assumed that

$$P_{LC}(z) = \frac{w_{LC}^3(z)}{H_{LC}}. \quad (48)$$

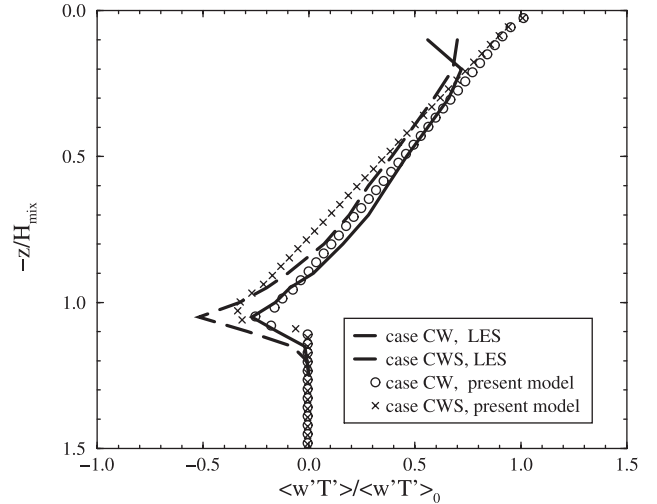


**Figure 6.** Comparison of heat flux profiles from the large-eddy simulations of *Skyllingstad and Denbo* [1995] and the present model. In case “CW” the Langmuir circulations were switched off, whereas in case “CWS” they were switched on. In both cases the ocean was forced with constant surface cooling and wind stress.

[44] Of course,  $H_{LC}$  is limited by the local water depth. This implies that the profile of  $w_{LC}$  is slightly different in shallower parts of the basin, such as near the coast. In that case, an area mean of  $P_{LC}$  should be calculated instead of as in equation (48). However, as long as the shallow fraction of the basin area is small compared with the total basin area, which is the case in the model domain, the hypsographic effects on  $P_{LC}$  may be neglected.

[45] To obtain a suitable value of  $c_{LC}$  in equation (46), we turn to the LES data of *Skyllingstad and Denbo* [1995]. They simulated the effect of including Stokes drift and the resulting LC in several idealized experiments. The initial condition was according to the Mixed-Layer Dynamics Experiment (MILDEX) [*Smith et al.*, 1987], that is, constant salinity, a 50 m deep surface layer of  $18.0^\circ\text{C}$  on top of colder water with a constant temperature gradient of  $0.2^\circ\text{C m}^{-1}$ . Various experiments of different forcings were performed, but here we will restrict ourselves to their cases “CW” and “CWS.” In both experiments the surface was cooled with a constant rate of  $160 \text{ W m}^{-2}$  and a constant wind stress of  $0.15 \text{ N m}^{-2}$ . The difference is that in case CWS the Stokes drift was switched on (hence the “S”) with resulting LC, whereas in case CW it was switched off.

[46] Figure 6 shows the profile of the calculated vertical heat flux  $\overline{w'T'}$  from the LES data of *Skyllingstad and Denbo* [1995] for the two cases after 8 hours of constant forcing, as well as the results with the present model. The LES data near the surface may be disregarded as they only show the resolved turbulent fluxes, not the subgrid-scale fluxes, which may be important near the surface [*Skyllingstad and Denbo*, 1995]. The depth and the heat flux in the figure have been nondimensionalized by division by the mixed layer depth  $H_{\text{mix}}$  and the surface heat flux  $\overline{w'T'}|_0$ , respectively.

[47] The results from case CWS with the present model are for  $c_{LC} = 0.15$ , which is a compromise between making

the curves fit at the base of the mixed layer and within the mixed layer. Using larger values (up to  $\sim 0.20$ ) gave better agreement at the base of the mixed layer but gave worse results within the mixed layer. Here we tentatively adopt the value  $c_{LC} = 0.15$ . The chosen value yields maximum vertical velocities  $w_{LC}$  of the order of a few centimeters per second, which is supported by the LES data of *Skyllingstad and Denbo* [1995].

## 5. Parameterization of Deep Mixing

### 5.1. Generation Mechanisms

[48] The part of the shear production of TKE due to subgrid-scale processes will here be denoted by  $P_{IW}$ , as it is expected to be mainly due to internal waves. In the world oceans,  $P_{IW}$  has a large contribution from the barotropic tide [Bell, 1975; Sjöberg and Stigebrandt, 1992], interacting with local topography to generate internal waves. The generated internal wave energy (IWE) is radiated away from the bottom and is dissipated elsewhere. If these near-bottom currents can be modeled accurately, then their contribution  $F_{\text{tide}}$  to the energy flux can be estimated as [Gill, 1982, p. 270]

$$F_{\text{tide}} = \frac{1}{2} \rho_0 [(N_b^2 - U_b^2 k_b^2)(U_b^2 k_b^2 - f^2)]^{1/2} U_b a_b^2. \quad (49)$$

In equation (49),  $N_b$  is the near-bottom buoyancy frequency,  $U_b$  is the magnitude of the near-bottom current,  $k_b$  is the dominating wave number of the bottom topography in the direction of the near-bottom current, and  $a_b$  is its amplitude.

[49] Internal waves are also generated by traveling wind patterns [Bell, 1978; D'Asaro, 1985; Nilsson, 1995]. One possible candidate is the interaction between turbulent eddies advected by wind-driven currents, which force vertical velocities in the pycnocline below the mixed layer. The resulting internal waves will have a frequency of the order of (but smaller than) the buoyancy frequency [Bell, 1978].

[50] *Weller* [1981] found observational evidence of downward propagating near-inertial internal waves, which he speculated were forced by wind-driven Ekman pumping in the thermocline. If the frequency  $\omega$  of the forcing is high enough ( $\omega > f$ ), internal waves will be generated with the same frequency.

[51] Baroclinic eddies, created by large-scale currents, represent another source of unresolved shear. Most of these eddies are probably generated in the near-surface layer where the currents are strongest but may be advected to greater depths along isopycnal surfaces. In the Baltic Sea, these eddies have been observed down to  $\sim 120$  m [Elken *et al.*, 1988; Kõuts, 1999], and their life time is probably of the order of several weeks. Their relative importance may be estimated as follows. The mean velocity of such an eddy is of the order of  $10^{-1}$  m s $^{-1}$  [Kõuts, 1999], which corresponds to a kinetic energy density of the order of  $10^1$  J m $^{-3}$ . According to observations from the Baltic Sea [Kõuts, 1999] they are typically 60 m thick and have a diameter of up to 20 km (a few internal Rossby radii). This implies a vertically integrated energy density of the order of  $10^2$  J m $^{-2}$ . If they dissipate their energy during several weeks, this corresponds to an energy flux density of  $< 10^{-4}$

W m $^{-2}$  per eddy. As the projected area of the eddies only occupies a fraction of the ocean, this implies that the mean contribution from the eddies corresponds to no more than  $10^{-5}$  W m $^{-2}$ . Though the eddies may be of importance locally, it seems that their contribution to the total energy budget is negligible. Hence in this study the effect of eddies is neglected.

[52] A third possible way of energizing the deep water is barotropic seiches due to pressure gradients arising from lateral sea level variations. These may in turn result from atmospheric pressure gradients or wind setup close to coasts. The generated bottom currents may then interact with the local topography and generate internal waves in the same manner as the barotropic tide does. The relative importance of this process is unknown.

[53] Globally, the tide and the wind seem to be of approximately the same importance, with mean energy fluxes of the order of  $10^{-3}$  W m $^{-2}$  [Bell, 1975, 1978; Munk and Wunsch, 1998]. As tides are negligible in the Baltic Sea, here we will only consider wind-forced internal waves. Regardless of the exact nature of the generating process, the IWE available for deepwater mixing in the Baltic Sea is expected to be correlated with wind energy. Using historical oceanographic data, it has been shown indirectly that this is indeed the case [Axell, 1998]. Hence in this investigation we will assume that the deepwater mixing is primarily wind driven.

[54] The energy flux from the wind to motions in the mixed layer can be calculated as  $\tau_i u_i$ , where indices  $i = 1, 2$  denote the  $x$  and  $y$  directions, respectively. Here we will assume that a fraction  $\Omega$  of the energy is transferred to the stratified ocean interior below, either by radiation of internal waves or by other processes:

$$F_{ml} = \max(\Omega \tau_i u_i, 0), \quad (50)$$

where  $F_{ml}$  is the energy flux density from the mixed layer, and the maximum function has been used to ensure that  $F_{ml} \geq 0$ , even though instantaneous values of  $\tau_i u_i$  may be negative (representing an energy flux from the ocean to the atmosphere). The exact value of  $\Omega$  varies in time and space, as it depends on the statistics of the wind forcing such as steadiness of wind patterns. *Stigebrandt* [1990] estimated this fraction as  $\Omega \leq 0.15$ , but we will tune it in section 6. The rest of the energy, the fraction  $(1 - \Omega)$ , is spent by working against buoyancy forces in the pycnocline or is converted to heat in the surface layer.

### 5.2. Vertical Distribution and Dissipation of IWE

[55] After being generated, the IWE is assumed to be temporarily stored in a pool of energy before it is dissipated to TKE. Let us denote the energy density by  $E(z)$  (unit: J kg $^{-1}$ ) and the vertically integrated pool of energy by  $E_0$  (unit: J m $^{-2}$ ), related to  $E$  through

$$E_0 = \frac{\rho_0}{A_0} \int_{-H}^0 E A dz. \quad (51)$$

Here we have neglected the small variation of density with depth.  $H = 250$  m is the basin depth,  $A = A(z)$  is the horizontal cross section, and  $A_0$  is the surface area of the basin. In this study we will have a prognostic equation for

$E_0$  rather than for  $E$  and then distribute the energy in the vertical using an empirical relation.

[56] The source term  $P_{IW}(z)$  must certainly depend on  $E(z)$  and  $E_0$ . Further,  $P_{IW}(z)$  also depends on the probability of the unresolved waves producing critical gradient Richardson numbers at level  $z$ . Here we will not attempt to calculate that probability, but we know from linear theory that the internal wave modulated Richardson number approaches critical levels as  $N$  increases [Stigebrandt, 1990]. As mentioned before, that the deepwater mixing depends on  $N$  does have some observational support [Moum and Osborn, 1986]. We may therefore expect a certain  $N$  dependence in  $P_{IW}$ , and here we will assume that

$$P_{IW}(z) = \frac{\alpha E_0 A_0 N^\delta(z)}{\rho_0 V \overline{N}^\delta}. \quad (52)$$

Here the coefficient  $\alpha$  has the dimension  $s^{-1}$ , and  $\delta$  is an empirical constant controlling the depth distribution of  $E$  [cf. Stigebrandt and Aure, 1989; Liungman, 2000]. Further,  $V$  is the total volume of the basin, defined as

$$V = \int_{-H}^0 A dz,$$

and  $\overline{N}^\delta$  is defined as

$$\overline{N}^\delta = \frac{1}{V} \int_{-H}^0 N^\delta A dz.$$

[57] It should be stressed that since  $V$  and  $\overline{N}^\delta$  both depend on the hypsographic function  $A(z)$ , so does  $P_{IW}(z)$ . However, this is the only way hypsography affects the internal wave mixing in this parameterization.

[58] Once we know  $P_{IW}(z)$ , we can calculate the corresponding normalized energy flux from the pool of IWE to the pool of TKE by integrating  $P_{IW}(z)$ :

$$F_{\text{deep}} = \frac{\rho_0}{A_0} \int_{-H}^0 P_{IW} A dz = \alpha E_0. \quad (53)$$

[59] The energy content  $E_0$  of the pool may be calculated from its sink and source terms. Here we will only consider one source term,  $F_{ml}$  from equation (50), and one sink term,  $F_{\text{deep}}$  defined by equation (53):

$$\frac{dE_0}{dt} = F_{ml} - F_{\text{deep}}. \quad (54)$$

[60] Other terms can easily be included, such as topographic generation of IWE due to, for example, tides or seiches producing near-bottom currents (see the discussion in section 5.1). In addition, we may consider including generation by wave-turbulence interaction and direct viscous dissipation. In this study we will settle with the two terms representing wind generation and wave-turbulence transfer, as they probably dominate the energy balance in the Baltic.

[61] Given the integrated energy content  $E_0$ , we know that the average energy density  $\overline{E}$  is  $E_0 A_0 / (\rho_0 V)$ . If the energy is

due to internal waves, we know from observations that  $E(z)$  is often proportional to the local buoyancy frequency,  $N(z)$  [see, e.g., Gill, 1982, p. 153]. Hence we assume  $E/N = \overline{E}/\overline{N}$  or

$$E(z) = \frac{E_0 A_0}{\rho_0 V} \frac{N(z)}{\overline{N}}, \quad (55)$$

where  $\overline{N}$  is the mean buoyancy frequency given by

$$\overline{N} = \frac{1}{V} \int_{-H}^0 N A dz. \quad (56)$$

### 5.3. Implications for Turbulence Dynamics

[62] Far below the mixed layer, in the absence of large-scale shear,  $P_s$ , the only source of TKE is breaking internal waves,  $P_{IW}$  (or possibly the shear from decaying baroclinic eddies). Assuming local balance in the TKE (equation (26)) between generation by breaking internal waves, buoyancy destruction, and viscous dissipation, we have

$$\varepsilon = P_{IW} + P_b. \quad (57)$$

As  $P_s$  and  $P_{LC}$  are zero or negligible here, from equation (34) we have  $R_f = -P_b/P_{IW}$ . Then we can write equation (57) as

$$\varepsilon = (1 - R_f) P_{IW}. \quad (58)$$

Further, using equation (29), we also have

$$K_h = \frac{R_f}{1 - R_f} \frac{\varepsilon}{N^2} \quad (59)$$

[cf. Osborn, 1980]. Now, combining equations (52), (58), and (59) leads to

$$\varepsilon = \frac{(1 - R_f) \alpha E_0 A_0 N^\delta}{\rho_0 V \overline{N}^\delta} \propto N^\delta, \quad (60)$$

$$K_h = \frac{R_f \alpha E_0 A_0 N^\delta}{N^2 \rho_0 V \overline{N}^\delta} \propto N^{\delta-2} \quad (61)$$

[cf. Stigebrandt, 1976; Stigebrandt and Aure, 1989].

[63] Different theories predict that  $1 \leq \delta \leq 2$  [Gargett and Holloway, 1984; Gregg, 1989; Gargett, 1990], but it seems difficult to distinguish between them using observational data.  $\delta = 1$  would imply that  $K_h \propto N^{-1}$ , which usually implies an increase of  $K_h$  with depth in the deep ocean. As mentioned above, this relation is often used to parameterize deep interior mixing [Gargett, 1984; Stigebrandt, 1987; Omstedt, 1990; Hu, 1996]. This has support from the measurements in the western North Pacific Ocean by Moum and Osborn [1986] as well as measurements in the Baltic Sea (H. U. Lass et al., manuscript in preparation, 2002), whereas the observations by Toole et al. [1994] from the North Atlantic and the North Pacific suggest  $\delta = 2$ . Here we will tune  $\delta$  for best model result when comparing with

**Table 3.** Summary of the Different Experiments

Experiment	LC	IWE	$\delta$	$F_0$ , $10^{-3} \text{ W m}^{-2}$	$\Omega$	$\Delta S_{\text{rms}}$ , psu
A	no	no	–	0.0	0.00	0.82
B	yes	no	–	0.0	0.00	0.82
C	yes	yes	1.1	0.9	0.00	0.18
D	no	yes	1.1	1.2	0.00	0.21
E	yes	yes	1.0	0.0	0.16	0.23

observations to determine an average value that suits the Baltic Sea best.

[64] A suitable numerical value of the coefficient  $\alpha$  encountered above can be estimated from equation (52). We see that  $\alpha^{-1}$  is the timescale over which the pool of energy is drained because of dissipation to turbulence. Here we will set  $\alpha = 1 \text{ day}^{-1} \approx 1.2 \times 10^{-5} \text{ s}^{-1}$ . It should be noted that the exact value of  $\alpha$  does not affect the long-term mean of  $F_{\text{deep}}$ , which is set by  $F_{ml}$ . However,  $\alpha$  sets the time lag between forcing and dissipation as well as the amplitude and transient behavior of  $E$ , a fact that could be used to tune  $\alpha$ . This will not be done here.

## 6. Results

### 6.1. Numerical Experiments

[65] The simulation period was 1 January 1985 to 31 December 1994. During this period the bottom water in the Baltic proper was stagnant the greater part of the time, but a few deep inflows occurred; see Figure 2. The period includes mild, normal, as well as severe ice winters [Omstedt and Nyberg, 1996; Omstedt and Axell, 1998] and should thus be fairly representative of today's climate. The details of the different numerical experiments are given below and are summarized in Table 3.

[66] An objective way of verifying the turbulence model is to calculate the root-mean-square (rms) difference between the observed and calculated salinity fields for a period of several years. This was accomplished by interpolating the observed and calculated salinity fields onto identical grids, with  $\Delta t = 0.1$  year and  $\Delta z = 5$  m. However, because an important deep inflow is missed by the model in early 1993 (see below), it was decided to include only the time period January 1985 to December 1992 in the rms calculations. Further, as there are some uncertainties regarding the horizontal homogeneity of the model domain with respect to freshwater spreading, it was decided to exclude the top 100 m in the rms calculations.

[67] In the first 10-year simulation, experiment A, the parameterized LC and IWE were turned off, that is,  $P_{LC} = 0$  and  $P_{IW} = 0$ . Thus because of the protecting halocline and thermocline, the deepwater mixing was only at molecular rates. The resulting salinity field is shown in Figure 7b, along with observations in Figure 7a. The deepwater salinity is constant until a deep inflow occurs in early 1994, and it is clear that the halocline depth soon becomes much too shallow. At the end of 1992, just before the great inflow of January 1993, the top of the halocline (here taken as the depth of the 8 psu isoline) is at  $\sim 90$  m according to observations. In experiment A the standard  $k$ - $\epsilon$  model predicts a depth of  $\sim 47$  m for the 8 psu isoline, that is, about half of the observed depth. The rms error in salinity was 0.82 psu for this experiment. See Table 3.

[68] In experiment B the LC were switched on, whereas the IWE was not. The result is shown in Figure 7c. The halocline depth is greater than before, but not deep enough compared to observations. At the end of 1992 the top of the halocline (8 psu) is now predicted to be at 55 m, that is, only slightly better than in experiment A. The rms error is 0.82 psu, just as in experiment A.

[69] In experiment C the LC were switched on as well as the IWE. As only few estimates of the deep long-term diffusivity in the Baltic proper are available, it was decided to tune the deepwater mixing scheme by minimizing the rms error in salinity. The energy flux  $F_{ml}$  from the mixed layer was set to the constant value  $F_0$ , which was varied in the range  $0.0 \leq F_0 \leq 1.4 \times 10^{-3} \text{ W m}^{-2}$  in steps of  $0.1 \times 10^{-3} \text{ W m}^{-2}$ . The parameter  $\delta$  was varied in the range  $0.5 \leq \delta \leq 2.0$  in steps of 0.1.

[70] When the salinity fields for the whole simulation period and the whole water column were compared, the smallest rms error was obtained with  $\delta = 1.1$  and  $F_0 = 0.8 \times 10^{-3} \text{ W m}^{-2}$ . However, excluding the last two years and the top 100 m from the rms calculation instead resulted in  $\delta = 1.1$  and  $F_0 = 0.9 \times 10^{-3} \text{ W m}^{-2}$ , which is adopted as the most suitable combination of  $\delta$  and  $F_0$  for the period; see Figure 8a.

[71] The resulting salinity field with  $\delta = 1.1$  and  $F_{ml} = F_0 = 0.9 \times 10^{-3} \text{ W m}^{-2}$  is shown in Figure 7d. The agreement is satisfactory, near the bottom as well as in the halocline, with  $\Delta S_{\text{rms}} = 0.18$ . The top of the halocline was now predicted at  $\sim 88$  m at the end of 1992, which is very close to observations (90 m). It can also be seen in Figure 7d that the parameterization of  $P_{IW}$  (equation (52)) yielded a certain seasonal variation in the deepwater mixing, in spite of the fact that  $F_{ml}$  was constant in this experiment. The reason is the occurrence of  $\bar{N}^\delta$  in the denominator in equation (52). Expressed differently, during the summer, some of the IWE is trapped in the thermocline, leaving less energy for the deep water.

[72] Also shown in Figure 7e is the resulting salinity field with the LC switched off (experiment D). The parameter  $\delta$  was again set to 1.1, but to obtain a reasonable salinity evolution near the bottom,  $F_0$  was increased to  $1.2 \times 10^{-3} \text{ W m}^{-2}$ . Comparing with Figures 7a–7d, we see that it is important to include both LC and IWE in ocean models when simulating the halocline depth on the timescale of several years. Without the LC the top of the halocline was predicted at only 66 m, even though the IWE had been increased by 33%. The rms error was 0.21 psu for this experiment.

[73] In experiment E the coefficient  $\Omega$  in equation (50) was tuned by again comparing salinity fields. The smallest rms error was obtained with  $\delta = 0.8$  and  $\Omega = 0.11$  if the whole water column and the whole period were included. If the last two years and the top 100 m were excluded from the data, the best result was obtained with  $\delta = 1.0$  and  $\Omega = 0.16$ ; see Figure 8b.

[74] Figure 7f shows the resulting salinity field from experiment E. The variability in the deep water increased compared with experiment C, but the result is not particularly better. The rms error for the lower 150 m for the period 1985–1993 (see above) increased from 0.18 psu to 0.23 psu, but the result is still reasonable. The top of the halocline was again successfully predicted, with the 8 psu isoline at  $\sim 90$  m at the end of 1992, exactly the same as observed.

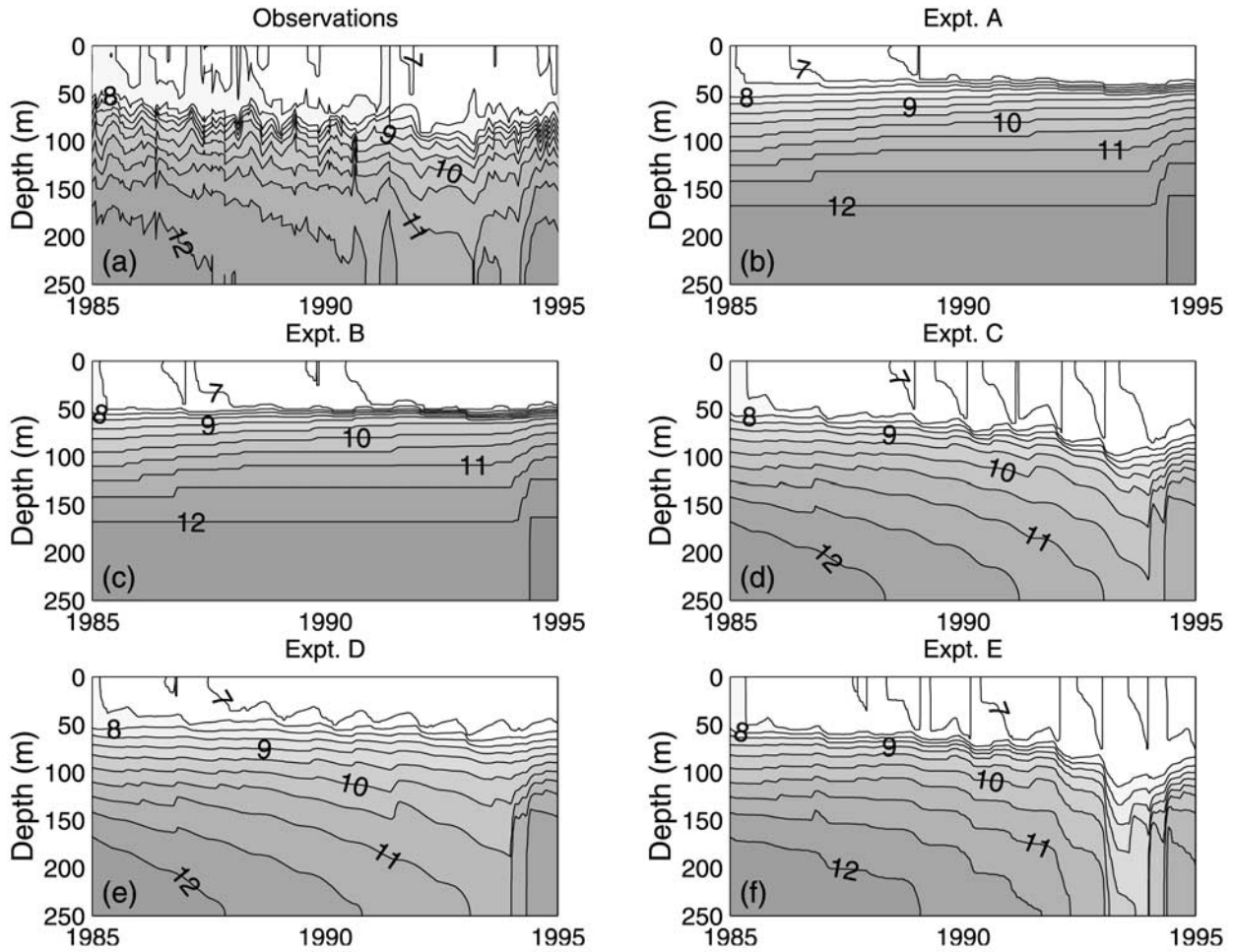


**Figure 7.** Observed and computed salinity fields. (a) Observed salinity field. (b) Result from experiment A in which LC and IWE were switched off. (c) Result after switching on the LC but with no IWE. (d) Result with both LC and IWE switched on ( $\delta = 1.1$  and  $F_0 = 0.9 \times 10^{-3} \text{ W m}^{-2}$ ). (e) Result with the LC switched off and the IWE retained ( $\delta = 1.1$  and  $F_0 = 1.2 \times 10^{-3} \text{ W m}^{-2}$ ). (f) Result with LC switched on and wind-dependent IWE ( $\Omega = 0.16$ ). See Table 3 for an overview of the different experiments.

[75] Summarizing the results from experiments C and E, an estimate of the uncertainty in  $\delta$  yields

$$\delta = 1.0 \pm 0.3.$$

For a given value of  $\delta$ ,  $F_0$  can be estimated with some precision, but there is still some uncertainty in  $F_0$  as it depends on the adopted value of  $R_f$ . Assuming that the deepwater value of  $R_f$  is known within, say, 30%, then

$$F_0 = (0.9 \pm 0.3) \times 10^{-3} \text{ W m}^{-2}.$$

A similar uncertainty is expected in  $\Omega$ , which yields

$$\Omega = 0.16 \pm 0.05.$$

[76] Figure 9 shows vertical median profiles of  $N$ ,  $E$ ,  $k$ , and  $\varepsilon$  from experiment E. According to the model, the IWE is proportional to  $N$  to match observations. Note that the absolute level of  $E$  depends on the model parameter  $\alpha$ , which has not been tuned in this model. As discussed

above, however, the long-term mean energy flux to the pool of TKE is set by  $F_{ml}$  and not by  $E$ . With  $\delta = 1.0$ ,  $k$  is independent of depth below the halocline ( $k \propto N^{+0.0}$ ), and  $\varepsilon$  is proportional to  $N$  below the halocline ( $\varepsilon \propto N^{+1.0}$ ); see Figure 9.

[77] The wind-dependent parameterization (equation (50)) in experiment E introduced interesting deepwater turbulence dynamics. This can be seen in Figure 10, which shows the logarithm of  $E$ ,  $k$ ,  $\varepsilon$ , and  $K_h$ . The example period is the sample year 1990. It can clearly be seen that all turbulence variables respond to the wind forcing. Further,  $E$  and  $\varepsilon$  are favored by the stratification. In contrast,  $k$  is independent of  $N$  below the halocline, and  $K_h$  is lower where  $N$  is high (in the halocline).

## 6.2. Comparison With Earlier Estimates

[78] Unfortunately, only a few estimates have been made of the actual eddy diffusivity below the halocline in the Baltic proper. However, the present author [Axell, 1998]

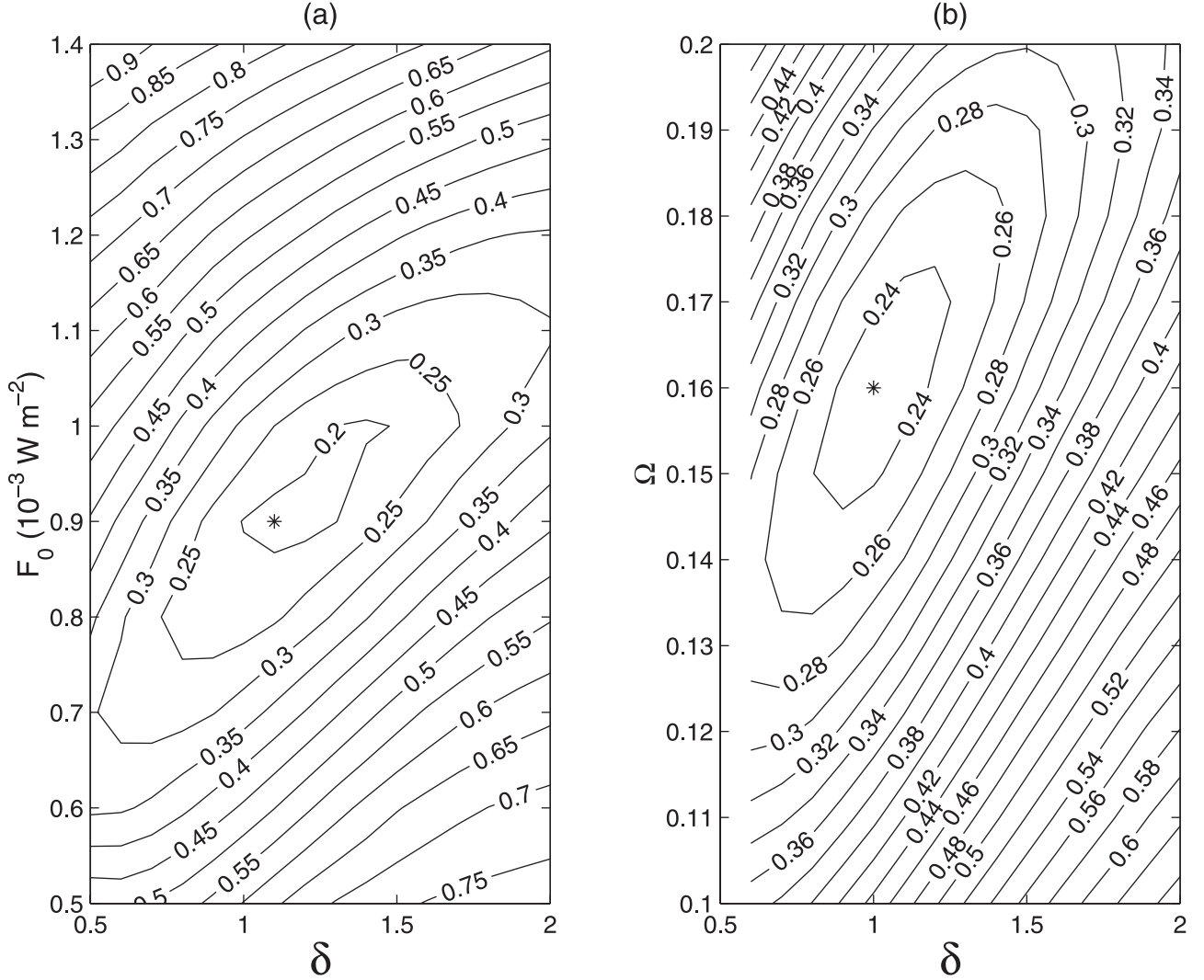


**Figure 8.** Rms errors for the salinity field (100–250 m depth, 1985–1993) for different combinations of  $\delta$ ,  $F_0$ , and  $\Omega$ . The stars (\*) mark the points with smallest rms errors. (a) Result from experiment C. (b) Result from experiment E.

made indirect estimates of the eddy diffusivity  $K_h(z)$  at BY15 (see the map in Figure 1), and the associated energy flux density  $F(z)$  was calculated with an expression equivalent to

$$F(z) = \frac{1}{A(z)} \int_{-H}^z R_f^{-1} K_h N^2 \rho A dz'. \quad (62)$$

The estimates of  $F$  from observations presented here have been recalculated with  $R_f = 0.08$  in the deep water to conform with the value assumed in this paper. From equation (58) and equation (59) we see that  $R_f^{-1} K_h N^2 = P_{IW}$ . Hence the model-calculated energy flux can also be calculated as

$$F(z) = \frac{1}{A(z)} \int_{-H}^z P_{IW} \rho A dz'. \quad (63)$$

All estimates of  $K_h$  and  $F$  are averages over periods of the order of weeks during 1985–1995; see Axell [1998].

[79] Figure 11a shows a comparison of all the (indirect) observations at the 150-m level during 1985–1995 with the corresponding values from experiment E.

[80] Figure 11b shows the corresponding comparison between the observed and modeled energy flux density  $F$  at the 150-m level, equivalent to the rate of work against the buoyancy forces below the 150-m level normalized with the horizontal cross section at the same level. Again, the result is very encouraging.

[81] Figure 12 shows a comparison of the long-term estimates from observations with model results from experiments C and E. The vertical median profiles of the diffusivity are shown in Figure 12a. The agreement with the indirect observations is very encouraging, but in experiment E the median diffusivity profile is somewhat low compared with experiment C and the estimate from observations. With  $\delta = 1.0$ ,  $K_h \propto N^{-1.0}$ , which is at least not contradicted by observations. Figure 12b shows the corresponding profiles of energy flux density  $F$ . Also here we see that the agreement with the indirect observations is

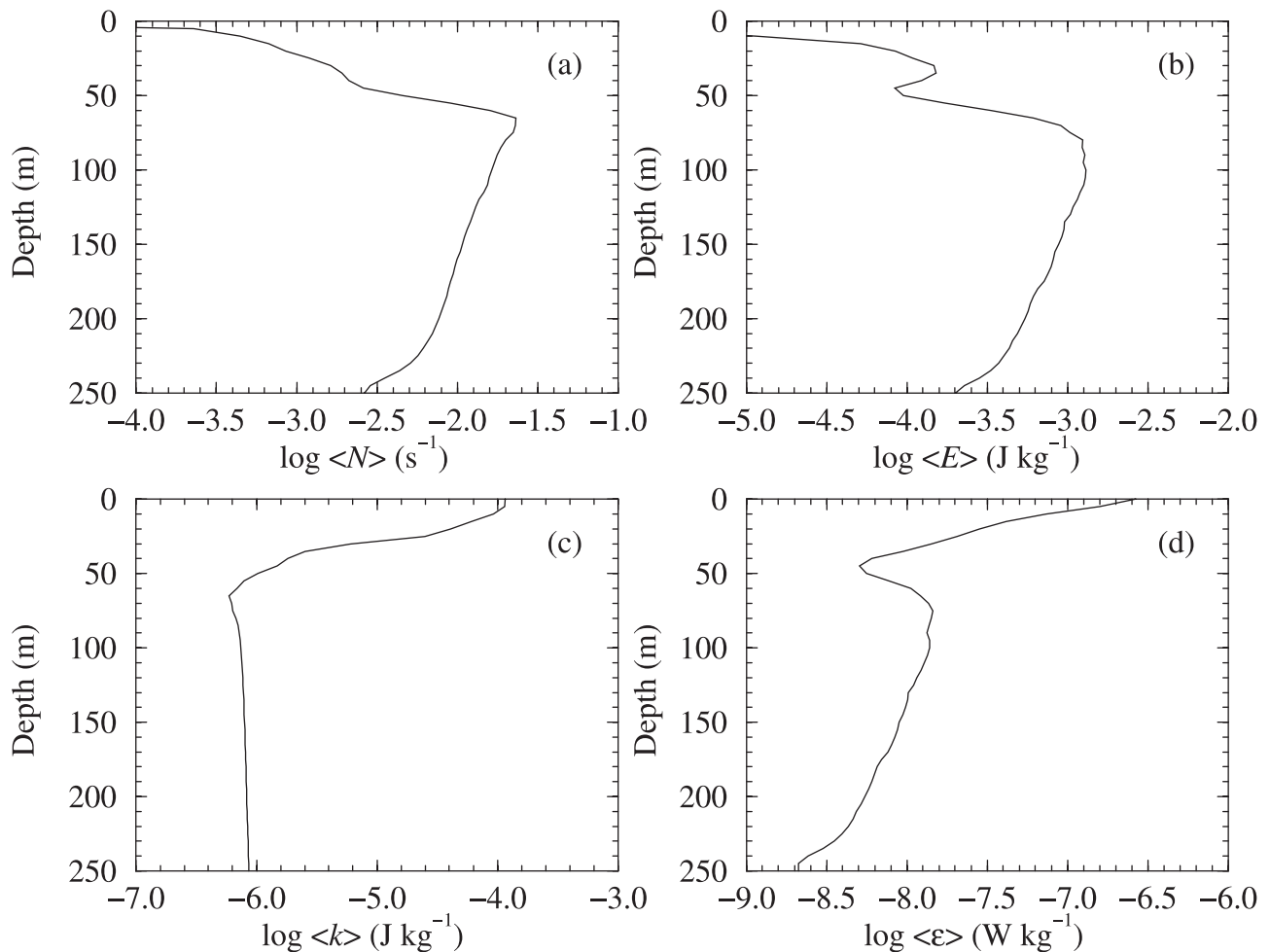


**Figure 9.** Long-term median profiles of (a) buoyancy frequency  $N$ , (b) internal wave energy density  $E$ , (c) turbulent kinetic energy density, and (d) dissipation rate of turbulent kinetic energy from experiment E.

good, but as in the case of  $K_h$  we see that  $F$  seems somewhat low in experiment E.

[82] The least squares fit of the data in Figure 11b seems to indicate that  $\sim 0.1 \text{ W m}^{-2}$  is not accounted for by the parameterization used in experiment E. Hence perhaps a better formulation of the energy flux is

$$F_{ml} = F_0 + \max(\Omega\tau_i u_i, 0),$$

with  $F_0 \approx 0.1 \times 10^{-3} \text{ W m}^{-2}$ . Figure 12 also seems to indicate that the energy flux is too small in experiment E, but this could also be explained by the variable nature of the wind-dependent mixing. As the energy flux is approximately proportional to the cube of the wind speed, most of the modeled energy flux to the deep water is supplied during relatively rare events with high wind speed. The result is a lower median profile in experiment E compared with experiment C in which  $F_{ml}$  was constant.

## 7. Discussion and Conclusions

[83] The difficulties of modeling the deep inflows, in spite of the use of observed salinity in the Bornholm Basin, is partly connected with the relatively poor temporal reso-

lution of the observations. Including the Bornholm Basin in the model domain would solve the sampling problem, but to model the salinity fluctuations in the Bornholm Basin correctly would require observations of the salinity in the Arkona Basin instead as a lateral boundary condition, as well as modeling of the dense bottom current between the Arkona Basin and the Bornholm Basin. The more upstream subbasins that are included in the model domain, the larger the uncertainty in the inflowing water into the Baltic proper. See *Omstedt and Axell* [1998] for an example of a multi-basin approach of modeling the whole Baltic Sea. Considering the difficulties in predicting the deep inflows into the Baltic proper, the overall result in the model runs presented here is judged to be satisfying.

[84] Langmuir circulations were accounted for by including a simple parameterization which involves the parameter  $c_{LC} = 0.15$ . A slightly larger value, closer to 0.20, gave better agreement with the LES data of *Skyllingstad and Denbo* [1995] in Figure 6 near the base of the mixed layer, but with worse agreement within the mixed layer. According to *Leibovich* [1983] we have

$$w_{LC} = cW,$$

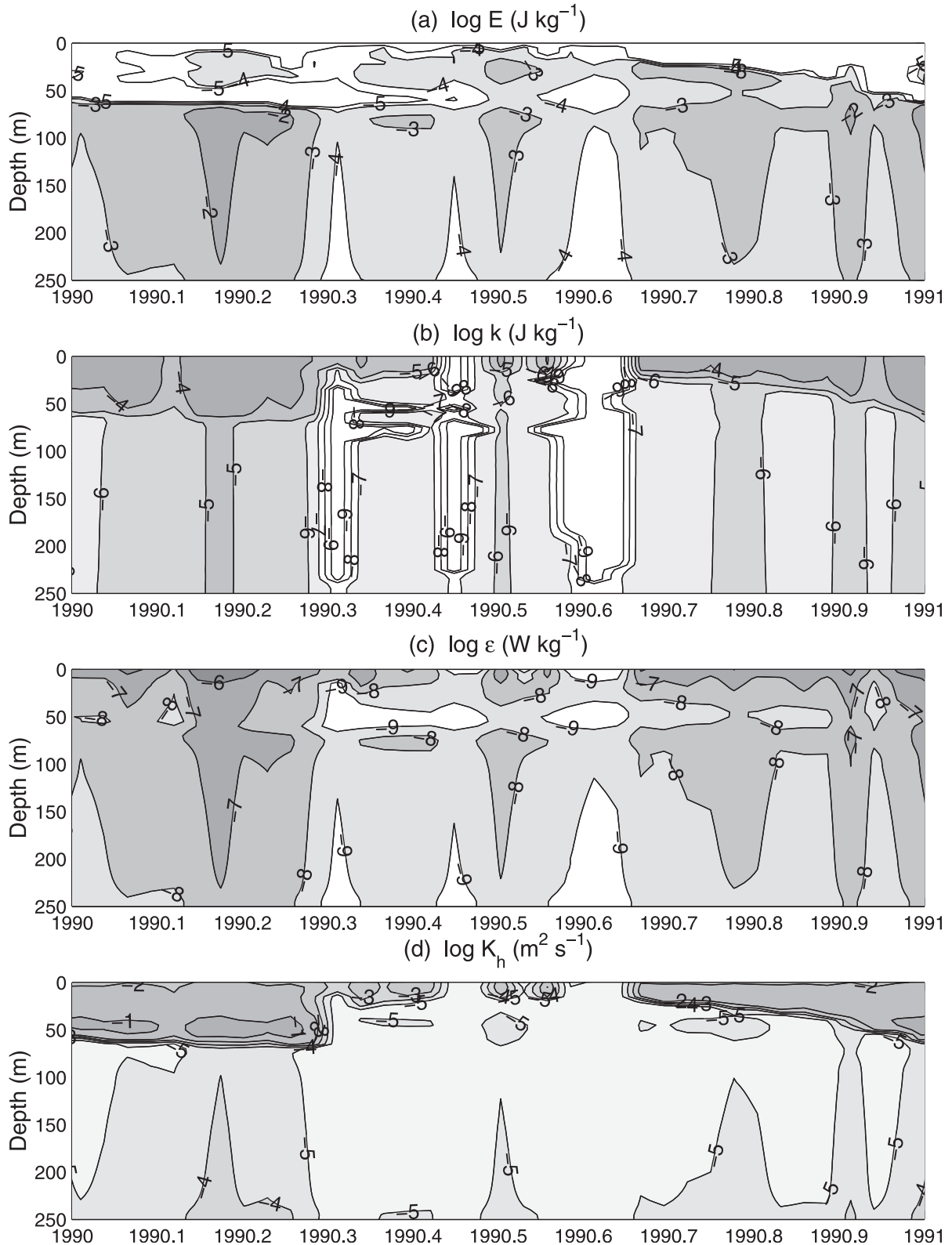


**Figure 10.** The logarithm of (a)  $E$ , (b)  $k$ , (c)  $\varepsilon$ , and (d)  $K_h$ , as calculated in experiment E for the year 1990. The effects of the wind forcing are clearly visible, even in the deep water.

with  $0.0025 < c < 0.0085$ . Combined with equation (44) we see that  $0.15 < c_{LC} < 0.54$ , which implies that the value used in this study (0.15) is at the lower end of the range. It should also be mentioned that the value of  $c_{LC}$

probably depends on the turbulence model used. However, with the one-equation  $k$  model of Axell and Liungman [2001],  $c_{LC} = 0.15$  gave results comparable with the present  $k$ - $\varepsilon$  model.

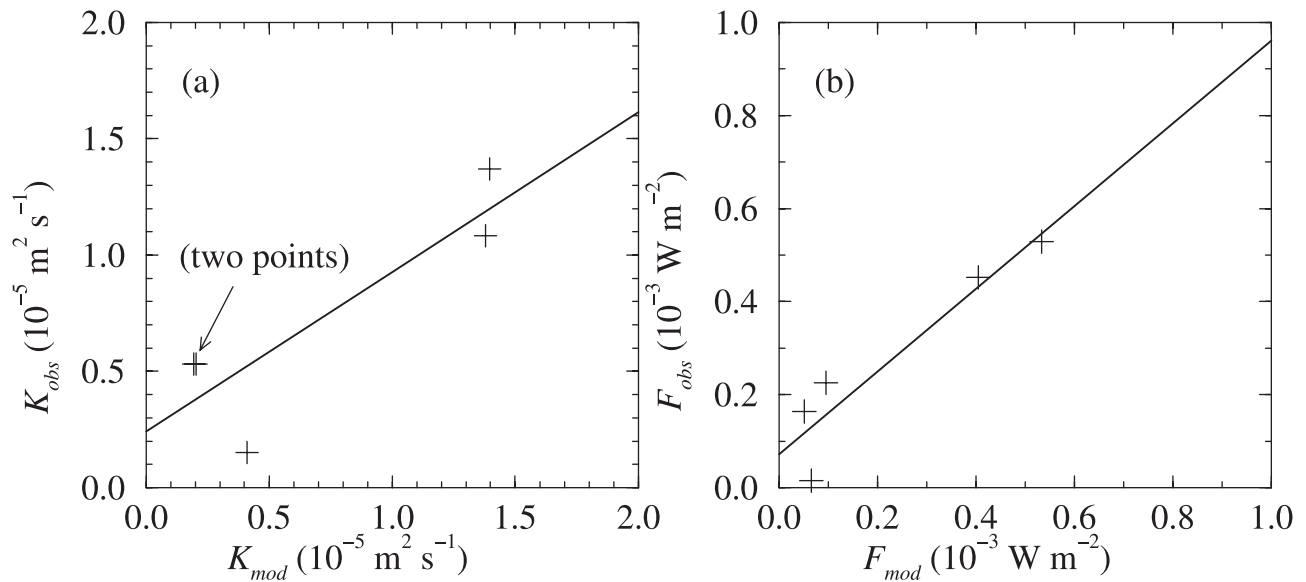


**Figure 11.** Comparison of observed [Axell, 1998] and calculated (experiment E) values of (a) eddy diffusivity ( $K_{obs}$  and  $K_{mod}$ ) and (b) energy flux density ( $F_{obs}$  and  $F_{mod}$ ) at the 150-m level. The lines indicate least squares fits to the data.

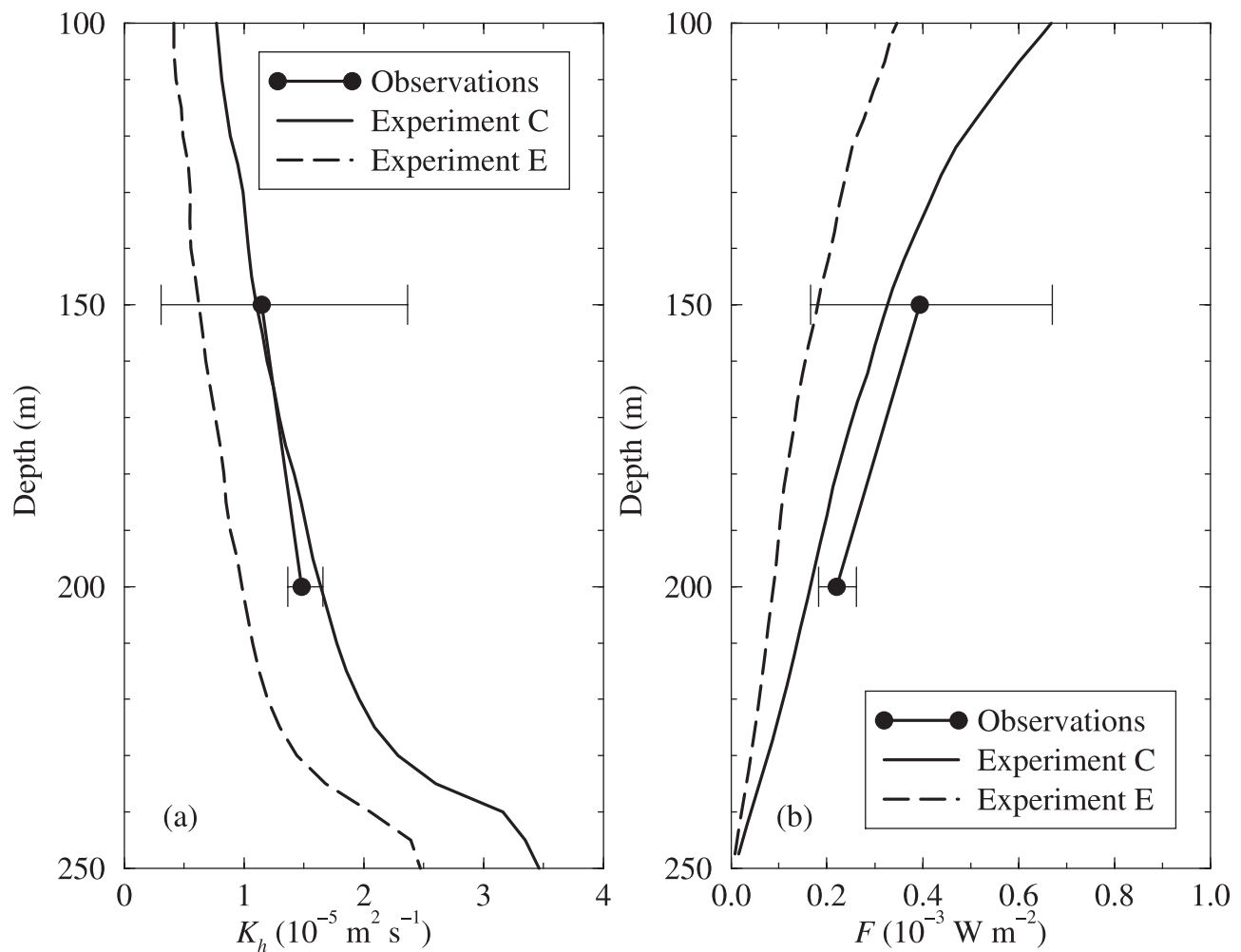


**Figure 12.** Long-term median profiles of observed and modeled (a) vertical diffusivity and (b) vertical energy flux density in the Baltic proper. The observations are from Axell [1998] and the model results from experiments C and E.

[85] In the simple internal wave model presented here, the energy available for mixing due to breaking internal waves was distributed according to  $P_{IW} \propto N^6$ . This empirical distribution of energy is, of course, a simplification, as it does not take into account increased levels of  $E$  due to local sources of internal waves. For example, observations in the world oceans show intensified mixing near rough topography [Polzin *et al.*, 1997; Stigebrandt, 1999], where the internal waves presumably are generated [Bell, 1975; Sjöberg and Stigebrandt, 1992].

[86] In experiment A it has been shown that, not surprisingly, standard turbulence models such as the  $k$ - $\epsilon$  model cannot describe turbulence outside the surface boundary layer, unless an extra source term of TKE is included. The reason is that in the absence of large-scale shear in the deep ocean, that is, below the surface boundary layer, the modeled TKE and the diffusivity fall to their prescribed minimum values. Whether the resulting diffusivity corresponds to laminar diffusion or some prescribed minimum mixing rate, the mixing is no longer controlled by the turbulence model itself and is therefore not likely to give physically sound results. In addition, the halocline depth became much too shallow when LC and IWE were neglected.

[87]  $F_0$  in experiment C has been tuned to represent today's climate. As the wind forcing may increase in strength during global warming because of, for example, increased storm frequency, a wind-dependent formulation of  $F_{ml}$  should be used. With the wind-dependent formulation of  $F_{ml}$  in experiment E, the energy flux is approximately proportional to the cube of the wind speed. The storms in early 1992 and 1993 gave too much energy to the deep water, which made the halocline too deep. One possible reason for this is that important inflows were missed around 1992–1993. Another possible reason is that the parameterization (equation (50)) has too strong a wind dependence. As the rms error was slightly larger with the present suggested formulation of a wind-dependent  $F_{ml}$  (equation (50)) than with a constant  $F_{ml}$ , a better wind-dependent formulation should be sought. For example, an indirect wind dependence can be obtained by making  $F_{ml}$  depend on the wind-driven currents and inertial oscillations. This may hopefully yield a proper seasonal variation.

[88] If the parameterization in equation (52) is to be used in a three-dimensional model, the ratio  $A_0/V$  can be substituted by  $H^{-1}$ , according to

$$P_{IW}(z) = \frac{\alpha E_0 N(z)}{\rho_0 H N},$$

where we have set  $\delta = 1$ . This implies that  $P_{IW}(z)$  is larger in shallower areas, for example near the coast. Other reasons for enhanced mixing in the coastal boundary layer are internal Kelvin waves and coastal jets. A combination of these factors may perhaps explain the increased mixing levels near the coast observed in, for example, Axell [1998].

[89] Finally, the tuning in experiment E resulted in  $\Omega \approx 0.16$ . This implies that  $\sim 16\%$  of the energy from the wind to the surface layer of the ocean is transported to the deep water, presumably by internal waves, where it performs the

observed deepwater mixing. For comparison, Stigebrandt [1990] estimated that  $\Omega \leq 0.15$ .

[90] An interesting question is whether it is the relatively large inflow of brackish water and freshwater into the model domain that makes it necessary to include Langmuir circulations in the modeling. To test this, a few extra 10-year simulations were made. Experiments C and D were simulated with the freshwater inflow reduced by 50% and were compared with the standard experiments C and D. However, neither the halocline depth nor the deepwater salinity changed at all compared with the standard experiments. The only visible changes were the sea surface salinity, which increased somewhat when the freshwater flow was decreased. Not even neglecting the freshwater flow totally (but retaining the brackish inflow,  $Q_{north}$ ) changed the results. Hence the results presented here do not seem to be sensitive to the amount of stabilizing buoyancy flux through the sea surface.

[91] The conclusions drawn from this study can be summarized in four main points: (1) Langmuir circulations and internal waves are important to include in Baltic Sea models intended for multiyear simulations. (2) The development of the salinity field in the southern Baltic Sea during 1985–1995 may be predicted with reasonable accuracy with  $\delta \approx 1.0$ , which corresponds to  $k \propto N^{0.0}$ ,  $\epsilon \propto N^{+1.0}$  and  $K_h \propto N^{-1.0}$ . (3) Approximately  $0.9 \times 10^{-3} \text{ W m}^{-2}$  is needed to explain the observed evolution of the deep salinity field in the Baltic Sea during 1985–1995 if  $R_f = 0.08$  in the deep water. (4) The wind-dependent forcing  $F_{ml} = \max(\Omega \tau_i u_i, 0)$  had a reasonable success in predicting the short-term as well as the long-term variability of the Baltic deep mixing during 1985–1995 with  $\Omega = 0.16$ , which means that 16% of the energy from the wind to the surface layer is transported to the deep water where it performs mixing.

[92] **Acknowledgments.** This work is a contribution to the Baltic Sea Experiment (BALTEX) as well as the Diapycnal Mixing Experiment (DIAMIX) and has been financed by the Swedish Meteorological and Hydrological Institute (SMHI). Thanks are due to Anders Omstedt, Anders Stigebrandt, two anonymous reviewers for comments on an earlier draft, and to Agneta Malm for technical assistance.

## References

- Arneborg, L., Oceanographic studies of internal waves and diapycnal mixing. Ph.D. thesis, Dept. of Oceanogr., Earth Sci. Cent., Göteborg Univ., Göteborg, Sweden, 2000.
- Axell, L. B., On the variability of Baltic Sea deepwater mixing, *J. Geophys. Res.*, *103*, 21,667–21,682, 1998.
- Axell, L. B., and O. Liungman, A one-equation turbulence model for geophysical applications: Comparison with data and the  $k$ - $\epsilon$  model, *Environ. Fluid Mech.*, *1*, 71–106, 2001.
- Bell, T. H., Topographically generated internal waves in the open ocean, *J. Geophys. Res.*, *80*, 320–327, 1975.
- Bell, T. H., Radiation damping of inertial oscillations in the upper ocean, *J. Fluid Mech.*, *88*, 289–308, 1978.
- Beszczynska-Möller, A., Transport of dense, near-bottom waters in the Stolpe Channel and related mesoscale hydrodynamic structures, in *Second Study Conference on BALTEX, Juliusruh, Island of Rügen, Germany*, edited by E. Raschke and H.-J. Isemer, Int. BALTEX Secr., GKSS Res. Cent., Geesthacht, Germany, 1998.
- Bougeault, P., and P. Lacarrère, Parameterization of orography-induced turbulence in a mesobeta-scale model, *Mon. Weather Rev.*, *117*, 1872–1890, 1989.
- Brown, R. A., Longitudinal instabilities and secondary flows in the planetary boundary layer: A review, *Rev. Geophys.*, *18*, 683–697, 1980.
- Bryan, F., Parameter sensitivity of primitive equation ocean general circulation models, *J. Phys. Oceanogr.*, *17*, 970–985, 1987.

- Burchard, H., and H. Baumert, On the performance of a mixed-layer model based on the  $k$ - $\epsilon$  turbulence closure, *J. Geophys. Res.*, *100*, 8523–8540, 1995.
- Burchard, H., and O. Petersen, Models of turbulence in the marine environment—A comparative study of two-equation turbulence models, *J. Mar. Syst.*, *21*, 29–53, 1999.
- Burchard, H., O. Petersen, and T. P. Rippeth, Comparing the performance of the Mellor-Yamada and the  $k$ - $\epsilon$  two-equation turbulence models, *J. Geophys. Res.*, *103*, 10,543–10,554, 1998.
- Craik, A. D. D., and S. Leibovich, A rational model for Langmuir circulations, *J. Fluid Mech.*, *73*, 401–426, 1976.
- Cummins, P. F., G. Holloway, and A. E. Gargett, Sensitivity of the GFDL Ocean General Circulation Model to a parameterization of vertical diffusion, *J. Phys. Oceanogr.*, *20*, 817–830, 1990.
- D'Alessio, S. J. D., K. Abdella, and N. A. McFarlane, A new second-order turbulence closure scheme for modeling the oceanic mixed layer, *J. Phys. Oceanogr.*, *28*, 1624–1641, 1998.
- D'Asaro, E. A., The energy flux from the wind to near-inertial motions in the surface mixed layer, *J. Phys. Oceanogr.*, *15*, 1043–1059, 1985.
- Deardorff, J. W., G. E. Willis, and D. Lilly, Laboratory investigation of non-steady penetrative convection, *J. Fluid Mech.*, *35*, 7–31, 1969.
- DeCosmo, J., K. B. Katsaros, S. D. Smith, R. Anderson, W. Oost, K. Bumke, and H. Chadwick, Air-sea exchange of water vapor and sensible heat: The HEXOS results, *J. Geophys. Res.*, *101*, 12,001–12,016, 1996.
- Eilola, K., and A. Stigebrandt, Spreading of juvenile freshwater in the Baltic proper, *J. Geophys. Res.*, *103*, 27,795–27,807, 1998.
- Elken, J., Deep water overflow, circulation and vertical exchange in the Baltic proper, *Rep. Ser. 6*, edited by J. Elken, 91 pp., Estonian Mar. Inst., Tallinn, Estonia, 1996.
- Elken, J., M. Pajuste, and T. Kõuts, On intrusive lenses and their role in mixing in the Baltic deep layers, paper presented at 16th Conference of the Baltic Oceanographers, Kiel, Germany, 1988.
- Gargett, A. E., Vertical eddy diffusivity in the ocean interior, *J. Mar. Res.*, *42*, 359–393, 1984.
- Gargett, A. E., Do we really know how to scale the turbulent kinetic energy dissipation rate  $\epsilon$  due to breaking of oceanic internal waves?, *J. Geophys. Res.*, *95*, 15,971–15,974, 1990.
- Gargett, A. E., and G. Holloway, Dissipation and diffusion by internal wave breaking, *J. Mar. Res.*, *42*, 15–27, 1984.
- Gill, A. E., *Atmosphere-Ocean Dynamics*, *Int. Geophys. Ser.*, vol. 30, Academic, San Diego, Calif., 1982.
- Gnanadesikan, A., Mixing driven by vertically variable forcing: An application to the case of Langmuir circulation, *J. Fluid Mech.*, *322*, 81–107, 1996.
- Gnanadesikan, A., and R. A. Weller, Structure and instability of the Ekman spiral in the presence of surface gravity waves, *J. Phys. Oceanogr.*, *25*, 3148–3171, 1995.
- Gregg, M. C., Scaling turbulent dissipation in the thermocline, *J. Geophys. Res.*, *94*, 9686–9698, 1989.
- Hu, D., On the sensitivity of thermocline depth and meridional heat transport to vertical diffusivity in OGCMs, *J. Phys. Oceanogr.*, *26*, 1480–1494, 1996.
- Ivey, G. N., and J. Imberger, On the nature of turbulence in a stratified fluid, part I, The energetics of mixing, *J. Phys. Oceanogr.*, *21*, 650–658, 1991.
- Kõuts, T., Processes of deep water renewal in the Baltic Sea, Ph.D. thesis, Institute of Environmental Physics, University of Tartu, Tartu, Estonia, 1999.
- Launiainen, J., Derivation of the relationship between the Obukhov stability parameter and the bulk Richardson number for flux profiles, *Boundary-Layer Meteorol.*, *76*, 165–179, 1995.
- Lehmann, A., A three-dimensional baroclinic eddy-resolving model of the Baltic Sea, *Tellus, Ser. A*, *47*, 1013–1031, 1995.
- Leibovich, S., The form and dynamics of Langmuir circulations, *Ann. Rev. Fluid Mech.*, *15*, 391–427, 1983.
- Li, M., and C. Garrett, Cell merging and the jet/downwelling ratio in Langmuir circulation, *J. Mar. Res.*, *51*, 737–769, 1993.
- Liljebadh, B., and A. Stigebrandt, Observations of the deepwater flow into the Baltic Sea, *J. Geophys. Res.*, *101*, 8895–8911, 1996.
- Liungman, O., Tidally forced internal wave mixing in a  $k$ - $\epsilon$  model framework applied to fjord basins, *J. Phys. Oceanogr.*, *30*, 352–368, 2000.
- Mellor, G. L., Retrospect on oceanic boundary layer modeling and second moment closure, paper presented at Fifth Aha Huliko'a Hawaiian Winter Workshop, Hawaii Inst. of Geophys., Honolulu, 1989.
- Mellor, G. L., and T. Yamada, Development of a turbulence closure model for geophysical problems, *Rev. Geophys.*, *20*, 851–875, 1982.
- Millero, F. J., Freezing point of sea water, *UNESCO Tech. Pap. Mar.*, *28*, 1978.
- Moum, J. N., and T. R. Osborn, Mixing in the main thermocline, *J. Phys. Oceanogr.*, *16*, 1250–1259, 1986.
- Munk, W., and C. Wunsch, Abyssal recipes, II, Energetics of tidal and wind mixing, *Deep Sea Res., Part I*, *45*, 1977–2010, 1998.
- Nilsson, J., Energy flux from traveling hurricanes to the oceanic internal wave field, *J. Phys. Oceanogr.*, *25*, 558–573, 1995.
- Nordblom, O., Numerical simulation of the atmospheric surface layer, M.S. thesis, Dept. of Environ. Eng., Div. of Water Resources Eng., Luleå Univ. of Technol., Luleå, Sweden, 1997.
- Omstedt, A., Modelling the Baltic Sea as thirteen sub-basins with vertical resolution, *Tellus, Ser. A*, *42*, 286–301, 1990.
- Omstedt, A., and L. B. Axell, Modeling the seasonal, interannual, and long-term variations of salinity and temperature in the Baltic proper, *Tellus, Ser. A*, *50*, 637–652, 1998.
- Omstedt, A., and L. Nyberg, Response of Baltic Sea ice to seasonal, inter-annual forcing and climate change, *Tellus, Ser. A*, *48*, 644–662, 1996.
- Omstedt, A., L. Meuller, and L. Nyberg, Interannual, seasonal and regional variations of precipitation and evaporation over the Baltic Sea, *Ambio*, *26*, 484–492, 1997.
- Osborn, T. R., Estimates of the local rate of vertical diffusion from dissipation measurements, *J. Phys. Oceanogr.*, *10*, 83–89, 1980.
- Plueddemann, A. J., J. A. Smith, D. M. Farmer, R. A. Weller, W. R. Crawford, R. Pinkel, S. Vagle, and A. Gnanadesikan, Structure and variability of Langmuir circulation during the Surface Waves Processes Program, *J. Geophys. Res.*, *101*, 3525–3543, 1996.
- Polzin, K. L., J. M. Toole, J. R. Ledwell, and R. W. Schmitt, Spatial variability of turbulent mixing in the abyssal ocean, *Science*, *276*, 93–96, 1997.
- Rahm, L., A note on some hydrographic properties of the Eastern Gotland Basin, *Beitr. Meereskd.*, *58*, 47–58, 1988.
- Rodi, W., *Turbulence Models and Their Application in Hydraulics—A State-of-the-Art Review*, Int. Assoc. for Hydraul. Res., Delft, Netherlands, 1980.
- Rodi, W., Examples of calculation methods for flow and mixing in stratified flows, *J. Geophys. Res.*, *92*, 5305–5328, 1987.
- Sjöberg, B., and A. Stigebrandt, Computations of the geographical distribution of the energy flux to mixing processes via internal tides and the associated vertical circulation in the ocean, *Deep Sea Res., Part I*, *39*, 269–291, 1992.
- Skyllingstad, E. D., and D. W. Denbo, An ocean large-eddy simulation of Langmuir circulations and convection in the surface mixed layer, *J. Geophys. Res.*, *100*, 8501–8522, 1995.
- Smith, J. A., R. Pinkel, and R. A. Weller, Velocity fields in the mixed layer during MILDEX, *J. Phys. Oceanogr.*, *17*, 425–439, 1987.
- Stigebrandt, A., Vertical diffusion driven by internal waves in a sill fjord, *J. Phys. Oceanogr.*, *6*, 486–495, 1976.
- Stigebrandt, A., A model for the vertical circulation of the Baltic deep water, *J. Phys. Oceanogr.*, *17*, 1772–1785, 1987.
- Stigebrandt, A., *Compendium on Marine System Analysis*, vol. 2, *Diapycnal Mixing in the Ocean (in Swedish)*, 65 pp., Dept. of Oceanogr., Göteborg Univ., Göteborg, Sweden, 1990.
- Stigebrandt, A., Baroclinic wave drag and barotropic to baroclinic energy transfer at sills as evidenced by tidal retardation, seiche damping and diapycnal mixing in fjords, paper presented at Aha Huliko'a, Dynamics of Oceanic Internal Gravity Waves, II, Hawaiian Winter Workshop, Univ. of Hawaii at Manoa, Honolulu, 1999.
- Stigebrandt, A., and J. Aure, Vertical mixing in basin waters of fjords, *J. Phys. Oceanogr.*, *19*, 917–926, 1989.
- Svensson, U., A mathematical model for the seasonal thermocline, *Rep. 1002*, Dept. of Water Resources Eng., Lund Inst. of Technol., Lund, Sweden, 1978.
- Svensson, U., PROBE: Program for boundary layers in the environment, System description and manual, *Rep. Oceanogr. 24*, Swed. Meteorol. and Hydrol. Inst., Norrköping, Sweden, 1998.
- Svensson, U., and J. Sahlberg, Formulae for pressure gradients in one-dimensional lake models, *J. Geophys. Res.*, *94*, 4939–4946, 1989.
- Toole, J. M., K. L. Polzin, and R. W. Schmitt, Estimates of diapycnal mixing in the ocean, *Science*, *264*, 1120–1123, 1994.
- Weller, R. A., Observations of the velocity response to wind forcing in the upper ocean, *J. Geophys. Res.*, *86*, 1969–1977, 1981.
- Winsor, P., J. Rodhe, and A. Omstedt, Baltic Sea ocean climate: An analysis of 100 years of hydrographic data with focus on the freshwater budget, *Clim. Res.*, *18*, 5–15, 2001.
- Wulff, F., and A. Stigebrandt, A time-dependent budget model for nutrients in the Baltic Sea, *Global Biogeochem. Cycles*, *3*, 63–78, 1989.